DEVELOPMENT OF A ^{1}H/^{31}P SPECTROSCOPY COIL CUSTOMIZED FOR CANINE MODELS OF MUSCULAR DYSTROPHY

A Thesis

by

JEREMY P. SIA

Submitted to the Office of Graduate and Professional Studies of
Texas A&M University
in partial fulfillment of the requirements for the degree of

MASTER OF SCIENCE

Chair of Committee,	Mary P. McDougall
Committee Members,	Jim X. Ji
	Kristen C. Maitland
Head of Department,	Anthony Guiseppi-Elie

August 2016

Major Subject: Biomedical Engineering

ABSTRACT

Duchenne’s Muscular Dystrophy (DMD) is a recessive disorder affecting one in every 3,600 males. The progressive disorder causes lifelong muscle degeneration and eventual death. As no cure is currently available, research in testing treatments for DMD is an area of substantial interest. Animal studies are a necessary and valuable precedent to clinical trials, providing information on experimental treatment response and phenotypic variations that the animal model may present. In evaluating disease progression during treatments, biopsies can provide very accurate results but are often considered unfavorable in DMD animal models due to their invasive nature.

^{31}P NMR spectroscopy provides a noninvasive means of quantifying concentrations of key muscle metabolites such as phosphocreatine (PCr) and inorganic phosphate (Pi). These metabolites can be used for characterizing disease progression in the Golden Retriever with Muscular Dystrophy (GRMD) canine animal model. While targeted GRMD muscle groups measure between 7 – 15 cm long, depending on the age of the animal model and the stage of the disease progression, commercially available coils capable of ^{31}P spectroscopy measure approximately 20 x 30 cm. This size difference causes a decrease in sensitivity and thus a decreased signal-to-noise ratio (SNR), motivating the need for a coil customized to interrogate this animal model effectively.

This thesis describes the design and development of a double-tuned ^{1}H/^{31}P coil customized for use on canine models of muscular dystrophy using a butterfly/loop configuration. The coil was first developed for a 4.7T Varian Inova scanner and later replicated for a 3T Siemens Verio scanner. Performance of both coils was analyzed using RF bench measurements to test for quality factor and tuning. The capabilities of the 4.7T coil were demonstrated through obtaining proton images and phosphorus spectra of a muscle phantom and canine muscle tissue samples from both control and dystrophin-deficient animal models. The results present a coil capable of obtaining localized and sensitive MR images and spectra using a size and geometry that is optimal for targeted GRMD muscle groups.

ACKNOWLEDGEMENTS

I would like to thank my committee chair, Dr. Mary McDougall, and my committee members, Dr. Jim Ji and Dr. Kristen Maitland, for providing me with support and advisement throughout the course of my Master’s program.

I would also like to thank my lab mates for allowing me to learn from you and enjoy your company throughout our graduate programs.

Thank you to John Sablan for your continual encouragement, patience, and jokes throughout both my college and graduate school programs.

Finally, thanks to my family for the guidance, perspective, and support you’ve given me throughout my life.

NOMENCLATURE

ADP	Adenosine Diphosphate
ATP	Adenosine Triphosphate
DMD	Duchenne’s Muscular Dystrophy
FID	Free Induction Decay
GRMD	Golden Retriever with Muscular Dystrophy
LNA	Low-Noise Amplifier
MRI	Magnetic Resonance Imaging
MRS	Magnetic Resonance Spectroscopy
NMR	Nuclear Magnetic Resonance
PCr	Phosphocreatine
Pi	Inorganic Phosphate
Q	Quality Factor
RF	Radiofrequency
Rx	Receive
TIPS	Texas A&M Institute for Pre-Clinical Studies
TR	Transmit/Receive
Tx	Transmit

TABLE OF CONTENTS

Page

LIST OF FIGURES

LIST OF TABLES

Page

CHAPTER I

INTRODUCTION

Nuclear magnetic resonance (NMR) spectroscopy is a technique used to noninvasively detect concentrations of different metabolites within the body. Many atoms are considered NMR-active because they possess a net charge that can be detected through the use of a radiofrequency (RF) coil. Some examples of NMR-active nuclei that are present in the body include ^{1}H, ^{13}C, and ^{31}P. This thesis focuses specifically on the development of a RF coil capable of ^{31}P spectroscopy and ^{1}H imaging to be used on canine animal models of muscular dystrophy.

I.1 Motivation

Duchenne's muscular dystrophy (DMD) is a recessive disorder affecting one in every 3,600 males. The progressive disorder causes lifelong muscle degeneration and eventual death. Life expectancy for those diagnosed is estimated to be approximately 25 years of age. Currently, there is no cure available. Certain trials have shown promise in slowing muscle degeneration, with subjects experiencing small clinical improvements in walking. Thus, research in developing cures and treatments for DMD is an area of substantial interest [1].

As a means to obtaining relevant information from clinical trials, animal studies are a necessary and valuable precedent. To be useful, this data must then be translatable, taking into account any phenotypic variations that the animal model may present. In studying disease progression of DMD in animal models, several methods are often used to characterize muscle metabolite concentrations including biopsies and clinical performance tests. Although biopsies provide very relevant and accurate information about a specific tissue, the results are highly localized and require invasive methods to obtain results, often damaging the existing tissue in the process and confounding longitudinal studies. In a muscular dystrophic animal model with sensitive muscle tissue, invasive methods are unfavorable for both the subject and the accuracy of the results. Clinical performance tests, although providing more general data concerning the entire organism, provide limited information concerning disease progression at the molecular level [2]. This creates a gap in testing DMD disease progression in animal models with a method that is noninvasive, spatially unrestricted, and capable of providing data at the histological level.

MR spectroscopy (MRS) can be used to noninvasively detect concentrations of different metabolites in the body. This technique utilizes the magnetic properties of a given nuclei to differentiate and quantify the organic constituents in the region of interest. A specified region is chosen from a “scout” or initial image of the subject and the tissue in this region is interrogated through MRS for different compounds and their relative concentrations. Since nuclei of the same element found in different molecular structures will have varying electron clouds, each nucleus will be shielded from the magnetic field to a greater or lesser extent, resulting in slight changes in the resonant frequencies observed, an occurrence known as chemical shift. This allows acquisition of a spectrum of radiofrequency signals with each peak corresponding to known metabolites and with the height of each peak representative of the metabolite’s relative concentration.

Several metabolites are of interest in DMD patients. Adenosine triphosphate (ATP), phosphocreatine (PCr), or inorganic phosphate (Pi) concentrations have been measured in recent studies through the use of ^{31}P spectroscopy [2]. Monitoring adjustments of these muscle metabolites in dystrophin-deficient animal models allows the evaluation of response to therapy. If these compounds can be accurately assessed through MRS and provide comparable information that correlates to that of a traditional method such as a biopsy, this data will support the use of MRS as an outcome measure for DMD disease progression in animal models. The most relevant animal models to date have been the *mdx* mouse and the canine phenotype: golden retriever with muscular dystrophy (GRMD) [2-4]. Both models have been used in identifying potential drug targets for treating DMD. Between the two, the canine phenotype more closely resembles the clinical presentation and disease severity of DMD present in humans [5-6]. A maintained colony of GRMD dogs exists at the Texas A&M University Veterinary School of Medicine. This work will be done in collaboration with this school on the 3T Siemens Verio scanner located at the Texas A&M Institute of Pre-Clinical Studies (TIPS).

Surface coils represent the preferred means of NMR spectral acquisition. A significant property of surface coils is that signal sensitivity is highly dependent on the geometry and size of the coil structure [7]. Since targeted muscle groups from the GRMD canine population measure between 7 – 15 cm long, depending on the age of the animal model and the stage of disease progression, an optimized surface coil should be within the same range for maximum sensitivity. The commercial coil for use with the 3T scanner at TIPS capable of ^{31}P spectroscopy measures approximately 20 x 30 cm. This size difference decreases sensitivity and thus signal-to-noise ratio (SNR), prompting the need for the development of a coil customized to interrogate this animal model effectively.

I.2 Thesis Chapters and Organization

This thesis first provides background information pertinent to the study in Chapter II. The disease DMD is further described along with why the need for developing a treatment exists. Animal models of the disease are discussed here along with the rationale behind choosing the GRMD animal model. NMR spectroscopy is detailed within the next section of the background, with a focus on ^{31}P spectroscopy and its applications. The final section of the background elaborates on RF coils, their use in NMR spectroscopy, and the type of coil developed for this study.

The remainder of the study is outlined in the following three chapters: Chapter III describes the construction of the ^{1}H/^{31}P double-tuned coil at 4.7T. The coil's design requirements can be found here, along with how those requirements were met. Tuning and matching methods are presented in this section, along with the bench measurements showing the quality factor of the coil. Procedures and details for interfacing this coil with the Varian Inova 4.7T system are found in the last section of Chapter III.

Chapter IV describes the construction of the ^{1}H/^{31}P double-tuned coil for the 3T clinical scanner. The information on this coil is presented in a similar fashion to Chapter III with the main difference being the system interface used. This coil is designed for use with the Siemens 3T system and thus has different procedures and details for interfacing. Chapter V outlines the experimental details used to test the performance of the coils. A description of the muscle phantoms used and the canine muscle tissue samples can be found in this chapter. Results from both MRI and MRS experiments are then presented. Chapter VI concludes the thesis with a discussion of the results, implications that can be made, along with recommendations regarding future work.

CHAPTER II

BACKGROUND

II.1 Duchenne's Muscular Dystrophy

II.1.1 Disease Characterization

Duchenne's muscular dystrophy (DMD) is an X-linked recessive disease affecting 1 in every 3,600-6,000 males. The progressive disorder causes lifelong muscle degeneration and eventual death. More specifically, DMD causes progressive dystrophy of certain muscle groups affecting organs such as the brain, eyes, and kidneys, and entire systems including musculoskeletal, gastrointestinal, respiratory, and cardiovascular [1]. Life expectancy for those diagnosed is estimated to be approximately 25 years of age. Currently, there is no cure available. Certain trials have shown promise in slowing muscle degeneration, with subjects experiencing small clinical improvements in walking [2]. Thus, research in developing cures and treatments for DMD is an area of substantial interest.

II.1.2 Animal Models

Dystrophin-deficient animal models have been used previously in identifying drug targets to treat DMD. Pre-clinical trials using these animal models allow testing of potential therapies prior to advocating their use in human clinical trials. To be useful, this data must be translatable, taking into account any phenotypic variations the animal model may present in comparison to the human manifestation of the disease. Thus, the etiology of various forms of dystrophin deficiency in different animal models has been extensively examined.

The two most relevant animal models include the mouse phenotype, *mdx*, and the canine phenotype, golden retriever with muscular dystrophy (GRMD). The disease progression and severity in GRMD animal models more closely resembles the condition presented in humans [3]. For example, the GRMD model still develops significant fibrosis where *mdx* mice presents a relative lack of fatty degeneration compared to DMD [4].

In studying the disease manifestation of this animal model, biopsies are commonly used to obtain information on muscle metabolites. While they provide accurate and relevant information, the findings are highly localized. In addition, biopsies can be considered unfavorable due to their invasive nature in a muscle degenerative animal model. MRS can potentially provide a method that is noninvasive, spatially unrestricted, and capable of providing data at the histological level.

II.2 NMR Spectroscopy

II.2.1 NMR Physics

The phenomenon known as NMR depends on the magnetic properties of the atomic nucleus. Specific atoms with an odd number of protons, will possess an angular momentum or “spin” that can create a magnetic field. While outside of a strong magnetic field, these spins will orient themselves in random directions as seen in Fig. 2.1.a, with no correlation to neighboring atoms. Placed within a strong magnetic field, with strength B_o, the nuclei will align their spin axes with that of the field. The torque exerted by the strong external magnetic field on the spinning nuclei produces a circular motion known as precession.

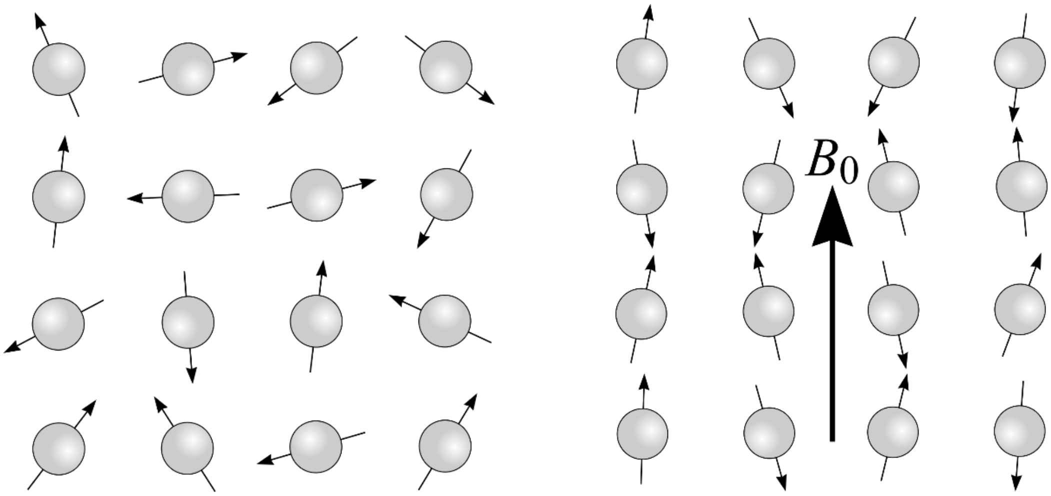

Figure 2.1 Spin Alignment. *(left)* Atomic nuclei with odd-number protons possess randomly oriented spins. *(right)* When placed in an external magnetic field, B_0, the spins align with the axis of the magnetic field causing precession [8].

The precessing nuclei shown in Fig. 2.1 show two sets of atoms –those aligned with the main magnetic field B_0 and those aligned against it. A slight excess of spins are aligned with the field, resulting in a net magnetization vector, often termed M_z because it points along the z-axis in conventional MR notation (the same direction as B_0). This net magnetization is the source of signal in an NMR experiment.

The frequency of precession plays a significant role in determining the results of the MR experiment. This value, ω, can be given by equation (2.1) shown below

$$\omega = \gamma B_0 \tag{2.1}$$

where γ is a constant known as the Larmor frequency which varies for different nuclei and B_0 is the strength of the external magnetic field to which the nuclei is exposed. Larmor frequency values given in MHz/T for various commonly interrogated nuclei can be found in Table 2.1.

Table 2.1. Larmor Frequencies and Natural Abundance of Common MR-Active Nuclei

Nucleus	Abundance (%)	γ (MHz/T)
^{1}H	100	42.5759
^{2}H	$1.5x10^{-2}$	6.5357
^{13}C	1.1	10.7054
^{14}N	99.6	3.0756
^{19}F	100	40.0541
^{23}Na	100	11.262
^{31}P	100	17.235

The net magnetization vector can be manipulated through a deposition of radiofrequency (RF) energy, or an RF pulse at the appropriate Larmor frequency. The nature of this RF pulse determines how the vector is manipulated. Fig. 2.2 below shows M_z pointing in the z-direction initially, the same direction as B_0.

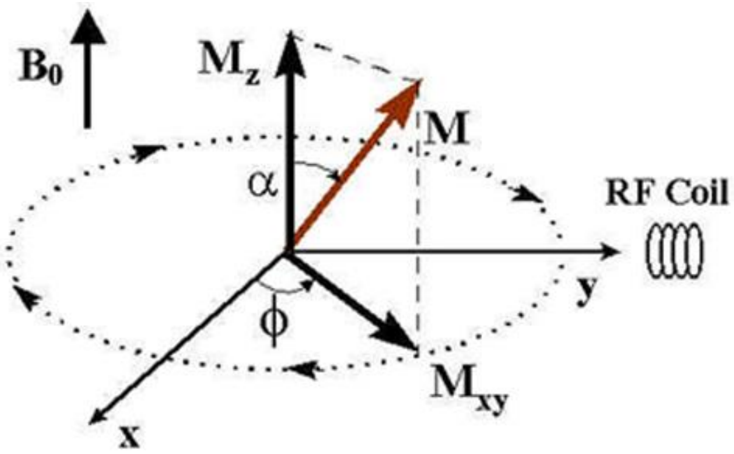

Figure 2.2 Magnetization Vector Manipulation. The net magnetization vector, M, aligns with the B_0 field initially and is termed M_z at this point. After deposition of energy through an RF pulse originating from a nearby RF coil, the magnetization vector can be tipped down into the x-y (transverse) plane, where it is shown as M_{xy} [9].

The RF pulse, denoted B_1, is generated with an RF "coil" as shown in Fig. 2.2. Once the pulse is applied, the magnetization vector M_z will be tipped by an angle α. The magnetization vector transverse to the B_0 field, M_{xy}, represents the source of our MR signal, as it becomes detectable by the nearby RF coil in this transverse plane. Thus, maximum signal is achieved when the entire M_z vector is tipped into the transverse plane ($\alpha = 90$ degrees). To achieve this, both the magnitude of the applied field and the duration of the RF pulse can be adjusted.

Once the RF pulse has tipped the magnetization vector into the transverse plane the magnetization vector will continue precessing at the Larmor frequency as shown by the dotted line in Fig. 2.2. This magnetization vector induces a voltage across a nearby receive coil through Faraday's law. The coil receives an RF signal at the Larmor frequency with an amplitude proportional to the magnetization vector's transverse component. Both of these properties can be seen in the original signal shown in Fig 2.3. The amplitude decreases over time showing a relaxation curve, while continuing to oscillate. Due to the nature of the curve, this signal is often termed the free induction decay (FID). This is the NMR signal that makes MRI and MRS possible.

By applying the Fourier transform (FT) to this signal, the spread of frequencies of the spins responsible for the decay of the FID can be seen, centered at the Larmor frequency. An illustration of this is shown in Fig. 2.3.

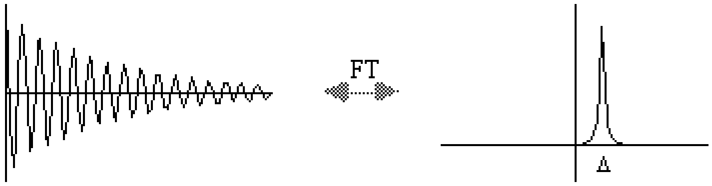

Figure 2.3 Fourier Transform of an NMR signal. The left shows an acquired NMR signal, the free induction decay (FID). The Fourier transform of this signal shows the spectrum of frequencies of the spins, centered at the Larmor frequency.

The nature of the FID produced does not rely solely on the nuclei being interrogated. Certain atoms will relax slower or precess faster based on the magnetic field it experiences from neighboring atoms within a molecule. These factors present varying resonant frequencies for similar nuclei found in different molecules. This occurs due to the electron shell each atom possesses. For example, a ^{13}C nucleus found in toluene (CH_3) will experience a different magnetic field than one found in benzene (C_6H_6). The magnetic field produced by the atom’s respective electron shell will shield each nuclei differently, and thus both will experience a subtle variation in the magnetic field present in the vicinity of the nucleus. This is called the chemical shift as it shifts NMR peaks to higher or lower frequencies, allowing different compounds to be identified and analyzed based on known electromagnetic properties of atoms. Because of this chemical shift, a spectra of compounds can be produced through MRS with multiple peaks corresponding to the concentration and properties of the interrogated nuclei.

II.2.2 Multinuclear Applications

As shown in Table 2.1, there are many different NMR-active nuclei on which MRS can be performed. ^{1}H is the most commonly used nuclei as it is found in water, which is highly abundant in our bodies. Through spatial localization of the NMR signal described above, an image can be produced. Because ^{1}H is 100% naturally abundant in our bodies, MRI of ^{1}H (proton imaging) provides very high soft tissue contrast which medical professionals can use for diagnostic purposes.

MRS of the NMR-active nuclei found in Table 2.1 can provide information useful for diagnosing and detecting abnormalities in metabolite concentrations found within the body. For example ^{13}C spectroscopy can be used in studying brain metabolism, analyzing metabolic exchanges between neurons [10]. Spectroscopy of ^{19}F is used to characterize pharmaceutical compounds and understand drug metabolism [11]. The nuclei under investigation in this thesis is ^{31}P and its applications will be presented in the next section.

II.2.3 ^{31}P Spectroscopy

MRS of ^{31}P is fairly common due to its 100% isotopic abundance and relatively high gyromagnetic ratio (3rd highest in Table 2.1 behind ^{1}H and ^{19}F). Phosphorus can be found in phospholipid bilayers and muscle metabolites such as adenosine triphosphate (ATP), inorganic phosphate (Pi), or phosphocreatine (PCr). MRS of these compounds allows pH, free adenosine diphosphate (ADP) and Mg^{2+} ion concentrations to be derived. ^{31}P spectroscopy has also been used in chemical analyses and to further understanding of skeletal muscles before and after muscle stimulation [12].

The use of this method in dystrophin-deficient models has also been performed, mainly studying ratios of PCr/ATP, PCr/Pi, Pi/ATP, or pH levels with focuses on the *mdx* mouse models [13, 14, 5]. Skeletal MRS studies of canids are still limited however. Some studies have been performed and show dystrophin deficient dogs had high resting Pi/PCr values compared with normal dogs [15].

The commercial RF coil available at the TIPS facility that is capable of performing ^{31}P spectroscopy measures approximately 20x30cm in size. If experiments are to be performed on these targeted GRMD muscles, which usually measure between 7 – 15 cm long, depending on the age of the animal model and the stage of the disease progression, then there is a need for a coil customized to interrogate this animal model more effectively.

II.3 RF Coils

As mentioned in the section on NMR physics, an RF coil is required to perform MRI/MRS. During transmit, the RF coil is used to apply an RF pulse to the sample. In this state, the RF coil is in transmit (Tx) mode. The applied pulse excites the NMR-active nuclei present in the sample, forcing a tipping of the magnetization vector into the transverse plane. Once this pulse is removed, the changing flux induces a current within the coil through Faraday induction. While the coil is receiving this signal, it is in receive (Rx) mode.

In this example, the coil used in Tx and Rx are one and the same. However, it is also possible for the Tx and Rx elements to be separate entities. In other words, one coil or coil array would be used to transmit RF energy, while another coil or coil array would be used to receive RF energy. This presents a flexibility to the design engineer to determine the optimal arrangement based on the properties of the specific application. For this study, two surface coils were used, both capable of transmitting and receiving RF energy.

II.3.1 Surface Coils

Surface coils represent a simple subset of RF coils used in MRI/MRS, but can obtain the highest sensitivity compared to other coil designs [16]. Their counterpart, the volume coil encloses the entire sample, providing less sensitivity but increasing field homogeneity. This homogeneity is sacrificed in surface coils to increase sensitivity and thus SNR in a localized region. A direct comparison between a volume and surface coil image of a phantom can be seen in Fig. 2.4 [17]. The properties of the image show that the field produced by the volume coil (left) is homogeneous as the SNR is uniform throughout. For the other image, a surface coil was used and the field pattern is not homogeneous, but rather localized near the coil. This maximizes the sensitivity in a region closest to the coil increasing the SNR drastically near the coil with signal drop off further from the coil.

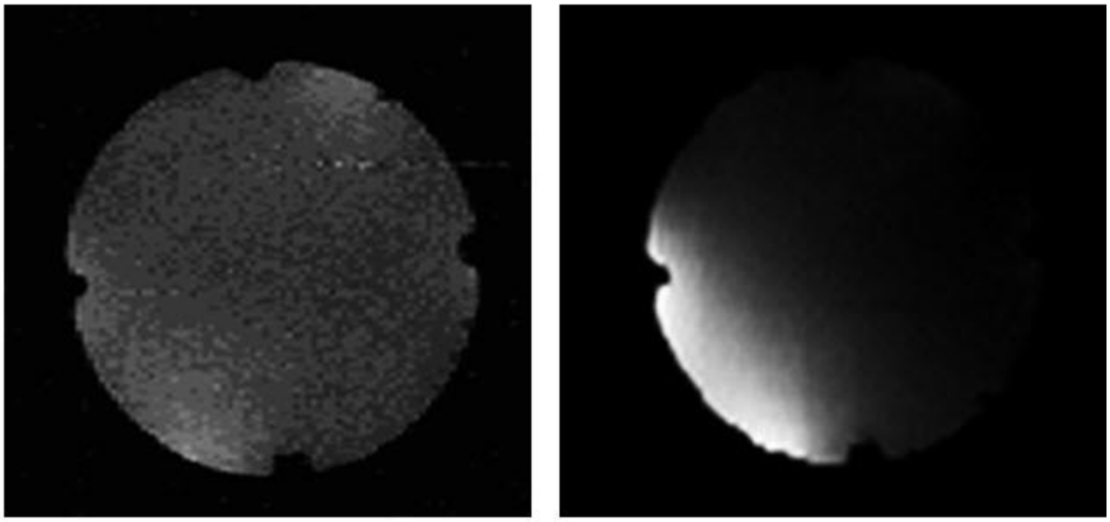

Figure 2.4 Image of a Homogeneous Phantom. *(left)* Image obtained using a volume coil showing a homogeneous field-of-view. *(right)* Image obtained using a surface coil showing a localized region with high SNR [17].

Although the signal acquired from either coil can be localized through the use of gradient coils, this does not apply to thermal noise. This suggests that a coil is sensitive to noise generated over the field-of-view it interrogates. In the example shown in Fig. 2.4, the phantom is homogeneous throughout. The volume coil obtains both signal and noise from the entire phantom producing the homogeneous image shown. By using a surface coil, thermal noise is only received from the region near the coil, which reduces the overall thermal noise and increases the SNR in the region of interest [18].

While increased SNR in a localized region is nearly always advantageous in receive applications, the tradeoff comes in the form of the inhomogeneous field during transmit. During transmit, the RF pulse is designed to create transverse magnetization. In the case of a surface coil, these tip angles will not be consistent over the entire sample due to the lack of homogeneity. The RF transmit power required to produce a given tip in one area of the sample will produce a greater rotation closer to the coil and a smaller rotation further from the coil. This produces the effect seen in Fig. 2.4.b where the intensity of the image is brightest in the regions closer to the coil, and darkest further away from the coil. Because of this, surface coils are designed for specific applications to ensure that the field-of-view is confined to the anatomy of interest.

The simplest surface coil structure is a simple loop. By running a current through a loop, magnetic field is created that is strongest in the center of the loop and becomes weaker moving away from the loop. The Biot-Savart law can be used to model the magnetic field produced by a loop using the equation (2.2):

$$\overrightarrow{dB} = \frac{\mu_0 I \overrightarrow{dL}\ x\ \overrightarrow{l_r}}{4\pi r^2} \tag{2.2}$$

where $\overrightarrow{dB}$ represents the magnetic field produced by an infinitesimal current element $\overrightarrow{dL}$. By integrating this over the length of the conductor, the magnetic field produced by the current carrying element can be modeled. In the case of a loop, the magnetic field pattern would look similar to the one shown in Fig. 2.5. The density of the lines in Fig. 2.5 correlates to the strength of the magnetic field pattern, with a stronger magnetic field produced closer to the coil as expected. Moving further away from the coil decreases the field strength exponentially, due to the r^2 term found in the denominator of equation (2.2).

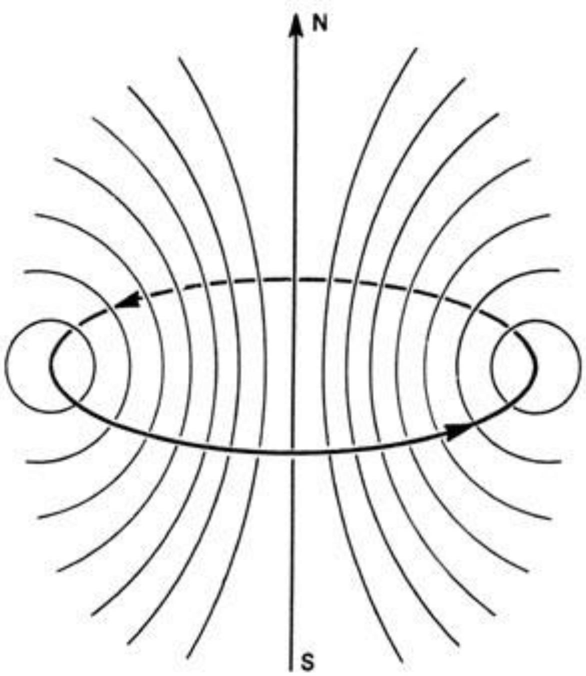

Figure 2.5 Magnetic Field Pattern of a Loop. Assuming a steady current, this image shows the field pattern produced by the loop [19].

Although the loop is the simplest surface coil structure, other configurations can provide various field patterns that can prove to be useful based on the application or anatomy of interest. For example, a pairing of two separate structures that produce orthogonal field patterns can help in decoupling two separate coil elements. This is the premise behind the use of the butterfly/loop structure discussed in the next section.

II.3.2 Butterfly/Loop Structure

Surface coil configurations can be chosen based on the specific application the RF coil will be used for. For this study, both ^{1}H and ^{31}P must be interrogated in the sample in order to produce proton images and ^{31}P spectra. The ^{1}H imaging capability will be used for acquiring a scout image that will allow us to ensure that we are acquiring signal from the area of interest. Once this has been accomplished, the coil must be able to acquire ^{31}P spectra without reconfiguring the setup between acquisitions. This will allow us to obtain a spectra from the correct region of interest.

Double-tuning a coil to be capable of acquiring signal from two separate nuclei, is a method often implemented in surface coils. Two key factors when double-tuning an RF coil include obtaining high sensitivity on the X-channel (the non-^{1}H channel) and achieving good isolation between the two channels. The first requirement exists due to the fact that between the two elements, ^{1}H is always more abundant and easily provides enough signal to produce good images or spectra. Thus, optimizing the X-channel is a priority between the two. The second requirement will ensure optimal SNR for both nuclei [7].

An excellent review of double-tuned coil construction is provided by Beck [20], but some specifics will be given here. Examples of implementations for double-tuning include the multiple-pole circuit, in which an additional resonant structure is placed in series with the coil's tuning capacitor, or a transformer-coupled circuit, in which two coils are purposefully coupled, causing a split in the frequency of interest into two separate frequencies. Although these configurations are common methods for double-tuning a coil, they can also lower Q values compared to their single-tuned counterparts. Both methods have also shown Q loss in the higher frequency modes, compared to the lower frequency mode of the coil [7]. An additional disadvantage presented by these methods is that using a single coil restricts the field-of-view for both elements to a single configuration.

To overcome these disadvantages, two separate coils tuned to different frequencies can be placed near the sample. The configuration used in this study is the butterfly/loop pair shown in Fig. 2.6.

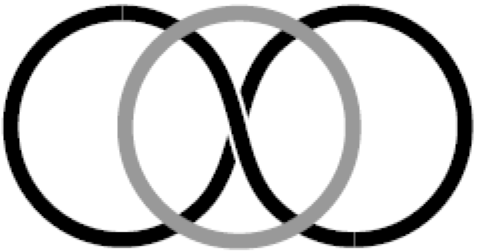

Figure 2.6 Butterfly/Loop Structure. The black lines represent the butterfly coil, while the gray lines represent the loop. Each element is tuned to a different frequency with perpendicular field patterns, allowing for inherent decoupling of the elements.

The configuration above is normally used to achieve quadrature for a single-frequency where both elements are tuned to the same frequency. Since the field patterns of both structures are perpendicular, this would allow the coil to increase the SNR by a factor of two during receive and also decrease the heating of the sample during transmit. However this is only one use of the butterfly/loop structure. Aside from a single-tuned quadrature coil, this configuration can also be used as a dual-resonant linear coil, the method used here to achieve ^{1}H and ^{31}P capabilities.

The advantage of this coil is in the nature of the flux generated between the two. Just like in the quadrature setup used for single-tuning, the two field patterns are still perpendicular for the double-tuned linear coils. Thus, the flux linkage between the coil pair is very low providing high isolation between the two channels [16]. Another advantage of this coil for this application is that the butterfly loop has a shallow field-of-view and is often used in applications where this is required. For the GRMD canine model, targeted muscle groups are superficial, making the butterfly coil favorable for encompassing the anatomy in its field-of-view.

CHAPTER III

CONSTRUCTION OF A $^{1}H/^{31}P$ COIL AT 4.7T

A double-tuned coil was required for this application to obtain ^{1}H images and ^{31}P spectra. Because availability to the 3T Siemens system was limited, the first iteration of this coil was designed and constructed for use on the Varian Inova 4.7T system located at the University Services Building. The whole project is separated into five stages which are outlined below. This thesis covers stages 1-3 in their entirety and introduces the steps required for stages 4 and 5.

- Stage 1: Design and construct $^{1}H/^{31}P$ coil for 4.7T
- Stage 2: Test and interface 4.7T coil on the Varian Inova system
- Stage 3: Design and construct $^{1}H/^{31}P$ coil for 3T
- Stage 4: Test and interface 3T coil on the Siemens Verio system
- Stage 5: Implement coil for *in vivo* studies

III.1 Design and Construction of the Multinuclear Transmit/Receive Surface Coil at 4.7T

The implementation of Stage 1 is achieved using the butterfly-loop surface coil from Fig. 2.6. Although this figure shows the basic butterfly structure, the dimensions can be optimized to maximize sensitivity as shown in Fig. 3.1.

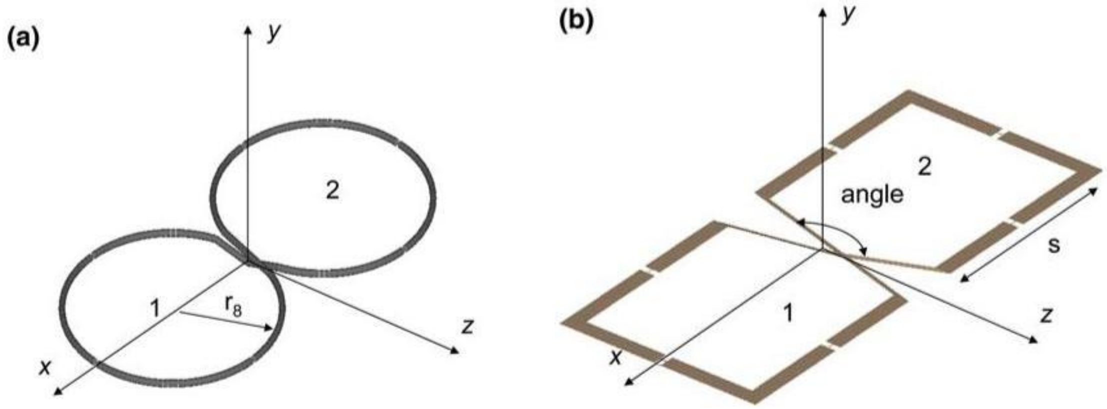

Figure 3.1 Two Configurations of the Butterfly Loop. a) Figure-8 loop of the butterfly coil. b) Square-shaped butterfly coil [21].

These geometries show dimensions that can be adjusted based on the imaging depth of the anatomy of interest. Because of the size of the pectineus muscle samples from the GRMD canine population, an imaging depth of 2.5 cm was chosen to maximize sensitivity. The square-shaped butterfly was originally chosen as the design, with a combination of the two geometries implemented in the final structure. The rationale behind this decision was that 3T was considered a high enough frequency that the sharp corners were rounded to prevent potential radiation losses. Modeling and experimentation was not performed to verify whether or not this was necessary.

Several important board dimensions include s, the side length, and r_0, the loop radius. In optimizing the structure, equation (3.1) describes the relationship between side length and depth of imaging, d [21]. As the muscle samples are approximately 2.5 cm thick on average and the coil is about 1 cm away from the samples, a depth of 3.5 cm was chosen to encompass the entire sample. Using equation (3.1), this yields to a side length of 4.16 cm, which was rounded down to 4.0 cm in the final coil construction.

$$s = 1.1d + 0.31 \tag{3.1}$$

The radius of the circular loop, r_0, to optimize SNR is based on the ratio from equation (3.2), which relates it to the side length [21]. Since s equals 4.0 cm, this yields a radius of ~3.0 cm for the circular loop.

$$\frac{s}{r_0} = 1.34 \tag{3.2}$$

The last parameter of importance is the crossover angle, α, of the two conducting lines in the center of the coil, where the condition from equation (3.3) must be met to maximize sensitivity from the coil [21].

$$\alpha \geq 150° \tag{3.3}$$

The design shown in Fig. 3.2 satisfies the three conditions outlined in the three equations above, using the parameters calculated. This board also implements the rounded edges mentioned previously. The whole board measures 7.5 cm in height and 11 cm in width. As the commercial coil available at the TIPS facility capable of ^{31}P spectroscopy measures approximately 20 x 30 cm, this board is approximately 37% of that size. The red trace representing the butterfly structure was tuned to the ^{1}H frequency at 4.7T (200.079 MHz) while the blue trace representing the circular loop was tuned to the ^{31}P frequency at 4.7T (81.005 MHz). These values were found using equation (3.4) which describe the resonance condition required to perform the NMR experiment for different nuclei based on their gyromagnetic ratio, γ, and the external magnetic field, B_0.

$$f = \gamma B_0 \tag{3.4}$$

The nuclei for each loop structure was assigned based on the 1st condition described in section II.3.2 to optimize double-tuned coils, where the X-channel sensitivity is prioritized. Since the circular loop is known to provide better sensitivity than the butterfly loop, this structure will be tuned for the X-channel which in this case is phosphorus.

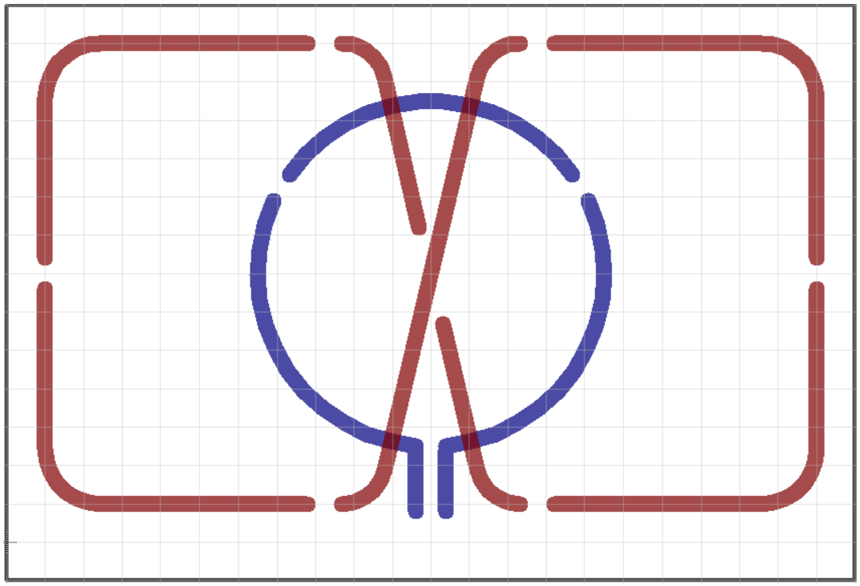

Figure 3.2 Butterfly/Loop Structure Design. This board shows the butterfly loop geometry using s = 4.0 cm, the circular loop using r_0 = 3.0 cm, and a crossover angle α = 152°. The red butterfly loop was tuned to the ^{1}H frequency while the blue circular loop was tuned to the ^{31}P frequency.

Construction of the double-tuned Tx/Rx butterfly/loop coil was implemented on flexible double-sided 0.41mm FR4 PCB board clad with 1 oz. of copper on each side (PCB

Depot, PN: 120802756087). A flexible board was chosen to ensure optimal anatomy coverage and subject comfort, as the end product is to be used on canine models *in vivo*. Although two single-sided boards could have been used, the double-sided copper-clad board provides for a more structurally sound and mechanically stable coil. The loop geometries were created in Eagle (version 7.2.0) and etched in-house using a protoboard machine (LPKF S63).

As can be seen in Fig. 3.2, standard distributed capacitance gaps were placed along the current path to ensure a uniform distribution of current for both loops. In the butterfly loop, a total of six gaps were used, while the circular loop used three gaps. In the center of the butterfly loop, copper tape of the same width as the trace was used to bridge the gap between the center trace while Kapton ® tape was used to insulate the two intersecting pathways.

Resonance was achieved by soldering surface-mount capacitors across the gaps. To achieve resonance, the capacitive reactance must cancel out the inductive reactance within the coil. Inductive reactance X_L is given by

$$X_L = \omega L \tag{3.5}$$

and capacitive reactance X_C is given by

$$X_C = \frac{-1}{\omega C} \tag{3.6}$$

where L is the coil’s inductance, C is the coil’s equivalent capacitance, and ω is a function of the frequency of interest given by equation (3.7).

$$\omega = 2\pi f \tag{3.7}$$

Therefore, the resonance condition is achieved when $X_C = -X_L$. Using equations (3.5) and (3.6), we arrive at equation (3.8) below.

$$\omega^2 LC = 1 \tag{3.8}$$

Since the inductance of the coil, L_{coil}, is a set value based on the geometry, trace width, and board material, we found L_{coil} for each loop by connecting a known capacitor in series with the loop and using S_{11} (reflection coefficient) measurements on the network analyzer to determine the resonant frequency of the loop. With both the resonant frequency and known capacitance, the value L_{coil} is easily solved for using equation (3.8). Once we calculated L_{coil} of the loop, we can use equation (3.8) again, this time inputting our desired frequency (200.079 MHz for ^{1}H and 81.005 MHz for ^{31}P) to solve for the equivalent capacitance required to achieve resonance. Table 3.1 shows the results of these tests.

Table 3.1. Resonance Requirements for ^{1}H/^{31}P Coil at 4.7T

	^{1}H Butterfly Loop	^{31}P Circular Loop
f_{res} (at 4.7T)	200.079 MHz	81.005 MHz
L_{coil}	534.23 nH	104.24 nH
$C_{equivalent}$	1.18 pF	37.04 pF

The equivalent capacitance values are distributed across the gaps shown in Fig. 3.2. Since the capacitors are considered to be in series, the capacitance required at each gap simply becomes $C_{equivalent}$ multiplied by the number of gaps. Thus, for the ^{1}H butterfly loop with six gaps, the capacitance used should be approximately 1.18 x 6 pF or 7.08 pF. As there are three gaps present in the ^{31}P circular loop, each capacitor should be approximately 37.04 x 3 pF or 111.12 pF.

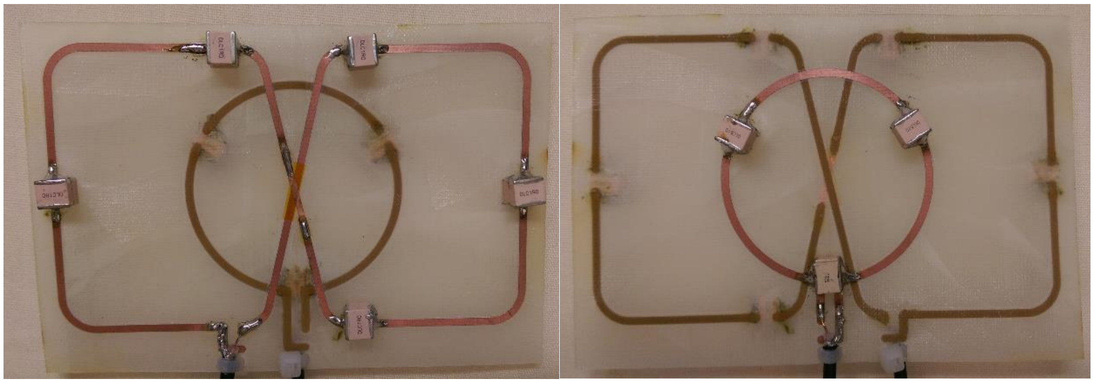

Figure 3.3 Implementation of Both Coils. The ^{1}H *(left)* and ^{31}P *(right)* coils can both be seen here after the distributed capacitors have been soldered on. The gaps shown help in creating a consistent current distribution around the coils.

As is standard practice, a variable capacitor was used in one gap for each of the loops to compensate for the variability in determining the L_{coil} value, ensuring maximum precision during the tuning process. These capacitors were chosen such that the desired capacitance value fell within the maximum and minimum values of its tuning range (Johanson Manufacturing PN: 55H01). Using a variable capacitor with a large range also provided flexibility in the capacitance values found in the other gaps. Instead of using exactly 7.08 pF for the ^{1}H loop or 111.12 pF for the ^{31}P loop, the capacitors used in the final implementation of this coil were 9.2 pF and 102 pF, respectively. These capacitors were acquired from PassivePlus, Inc. (2225C series) and are non-magnetic.

Once the coil was resonated at the correct frequency, the coils were impedance matched to 50 Ω. As illustrated in Fig. 3.4, both the resistance R and reactance X make up the coil's impedance Z.

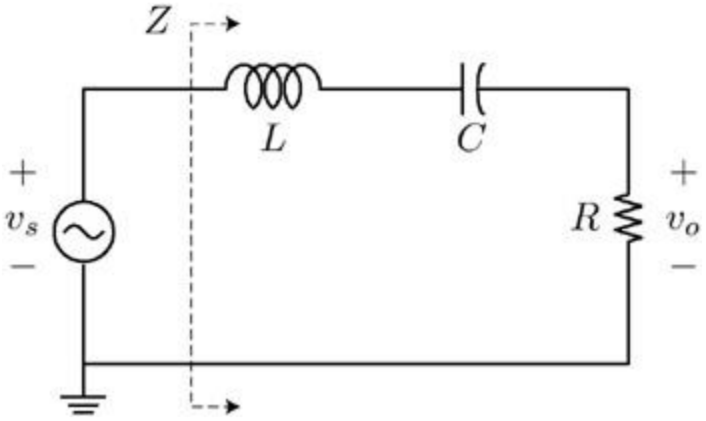

Figure 3.4 Standard Coil Represented as a Series RLC Circuit. The impedance Z is composed of the resistance R (real part) and the reactance X (imaginary part) which is a function of the inductance and capacitor values, L and C.

Because the resistance represents the real part and reactance represents the imaginary part of a coil's impedance, it is often represented as $Z_{coil} = R_{coil} + jX_{coil}$. In tuning the coil to a specific resonance, R_{coil} is transformed to 50 Ω. In matching the coil the remaining reactance must be cancelled such that $X_{coil} = 0$. This is achieved by adding an additional variable "matching" capacitor in series with the coil's signal line. For this coil implementation, the same types of variable capacitors used for tuning the coils were used as matching capacitors (Johanson Manufacturing PN: 55H01).

In order to allow the board to conform to the sample, the matching and tuning variable capacitors were placed off of the board in two enclosures, one for each loop. At 4.7T, both enclosures were only 1/40 of wavelength from the coil. The enclosures add mechanical stability and electromagnetic shielding to the coil design and house both the tuning capacitors and matching capacitors. The enclosures are pictured in Fig. 3.5 with both of these capacitors inside. The capacitors are soldered onto a PCB circuit board designed in Eagle and etched in-house (LPKF ProtoMat S-63). The boards used were single-sided FR4 with 1.524 mm board thickness (Electronix Express PN: P7BS17). They were connected to the resonant coil through the use of RG-174 cable (Belden 7805).

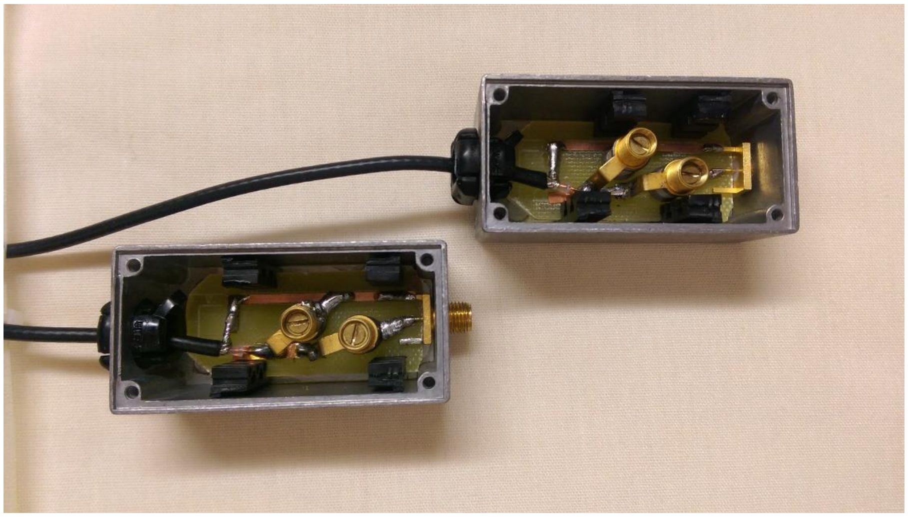

Figure 3.5 Enclosures Used to House Tuning and Matching Capacitors. The tuning and matching capacitors were housed in non-magnetic metal enclosures off of the board to maintain coil flexibility.

Once the enclosures were completed, baluns were added as the next component in the transmission line to achieve balanced currents on the center conductor and shield. In a balanced line, the current flowing on the inside of the shield and the outside of the center conductor are equal and opposite. Because they oppose each other, this prevents any external radiation, noise, or extra heating from being produced. This is called a differential mode current, and is desired for the entire length of the transmission line after the balun is added [22].

However, when a current flows on any portion of the transmission line without a nearby opposing current, this unopposed current is called a common mode current. These common mode currents can increase external coupling and radiation from the transmission line, leading to noise, decreased signal, and in some extreme cases, RF burns [22]. The addition of a balun tuned to the desired frequency of its transmission line inserts a large amount of impedance for the common mode current, reducing the undesired effects mentioned previously. This leads to a balanced line where the differential mode current dominates the common mode current along the length of the transmission line.

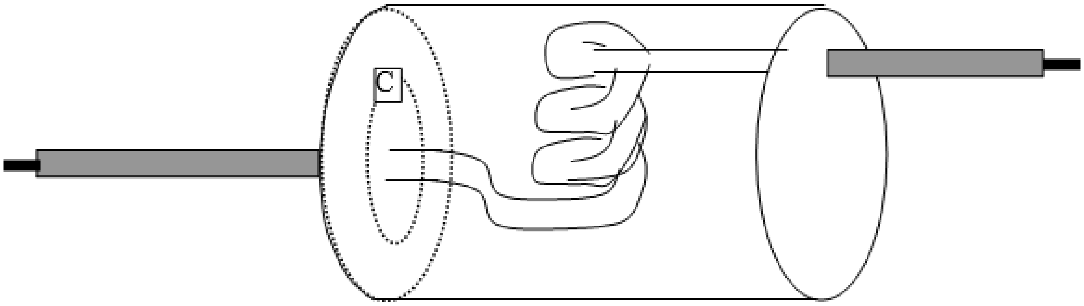

Figure 3.6 Balun Configuration. This circuit shows the basic idea behind transforming a unbalanced common mode current into a balanced differential mode current. The LC circuit works by “trapping” the undesired common mode current at a specific frequency.

The baluns used for this coil implementation are termed “can” baluns because of their cylindrical shape. They were created entirely in-house using 22 mm diameter PVC cylinders as the support structure. The inductor was created using semi-rigid coaxial cable wound around a 0.5 cm diameter plastic insulator. The insulator was removed once the solenoid was created. Before winding the semi-rigid coaxial cable, heat shrink was applied to the shield to prevent conductivity between the loops. A total of five turns were used. After inserting the wound solenoid into the PVC cylinder, PCB-printed end caps were set at each end. These end caps were created in Eagle software and etched on the LPKF S63 machine. They served to shield the inner inductor and hold the solenoid in place. A shield was created around the PVC cylinder using copper tape that was soldered directly onto the shield of the semi-rigid co-axial cable. To complete the mechanical structure of the balun, SMA male connectors were added to both sides of the semi-rigid coaxial cable (Amphenol PN: #132113). An adapter was also added that allowed the far end of the balun to connect to any system through an SMA female-female connection (Amphenol PN: #132169). Two of these balun structures were created for each of the two frequencies of the coil.

The next step for completing the baluns was tuning them to their respective frequencies. The solenoid possessed inductance according to equation (3.8) , leading to the capacitance values that should be used to tune to the desired frequencies. Table 3.2 below shows the intrinsic inductances of each balun and capacitance values used to tune them to their respective frequencies.

Table 3.2. Component Values of 4.7T Coil Baluns

	^{1}H Butterfly Loop	^{31}P Circular Loop
f_{res} (at 4.7T)	200.079 MHz	81.005 MHz
L_{balun}	5.86 nH	35.7 nH
C	17.4 pF	108 pF

The capacitors were soldered between the semi-rigid coaxial shield and the shield surrounding the PVC cylinder. This created the high impedance trap for the common mode currents. Fig. 3.7 shows the completed baluns developed and tuned for each of the two frequencies.

Figure 3.7 Baluns Tuned to the ^{1}H and ^{31}P Frequencies for 4.7T. These are 200.079 MHz and 81.005 MHz, respectively.

The completed coil is shown in Fig. 3.8. The butterfly/loop coil is shown at the end. The platform the coil sits upon is designed to allow the coil to sit in the center of the 40 cm diameter bore of the 4.7T Varian Inova system. In addition, the platform is long enough to support the tuning & matching network enclosures. An additional platform was created to place samples and phantoms for imaging and spectroscopy that can be lowered and raised for coil insertion and phantom placement.

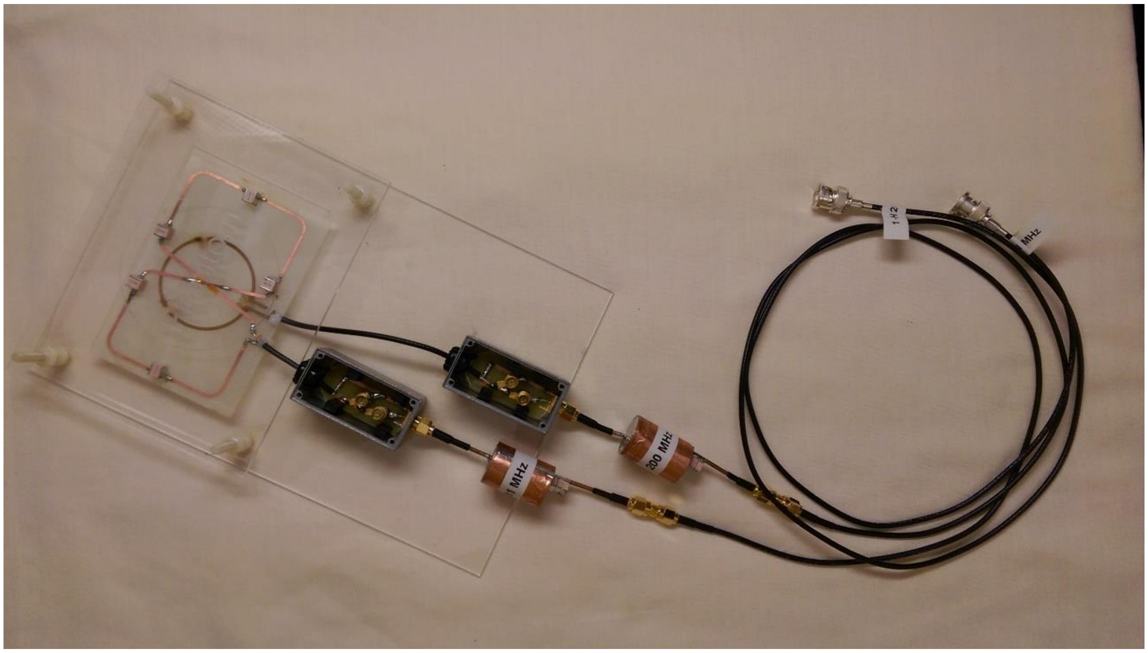

Figure 3.8 Final Implementation of the double-tuned $^{1}H/^{31}P$ coil for 4.7T. Tuning & matching networks and baluns have been removed from the coil structure, and cabling has been added to reach the flange plate at the end of the bore. An additional platform is set above the coil for phantom or sample placement.

III.2 Bench Measurements

III.2.1 Tuning and Matching

Tuning and matching are achieved through the use of the capacitor network described in the previous section. Recall that tuning transforms the resistance of the coil (R_{coil}) to 50 Ω. Once this is complete, a matching network that removes the remaining reactance of the coil, setting X_{coil} to 0. Thus, the desired impedance of the coil, Z_{coil}, after both tuning and matching is described in equation (3.9).

$$Z_{coil} = 50 + j0\,\Omega \tag{3.9}$$

To transform the resistance of the coil to 50 Ω, the equivalent capacitance required to achieve this must first be found. Since, for example, the butterfly coil had 6 gaps, we first shorted each of the gaps except for one using copper tape, and added a capacitor across the last gap. This initial capacitor value is arbitrary as it will only be used to find the coil's inductance using equation (3.8). Once the gaps have been shorted and a capacitor has been added across the last gap, we now have a resonant structure. Assuming the capacitor has value C_1, we only now need to find what frequency the coil is currently resonating at. This is achieved using S_{21} measurements.

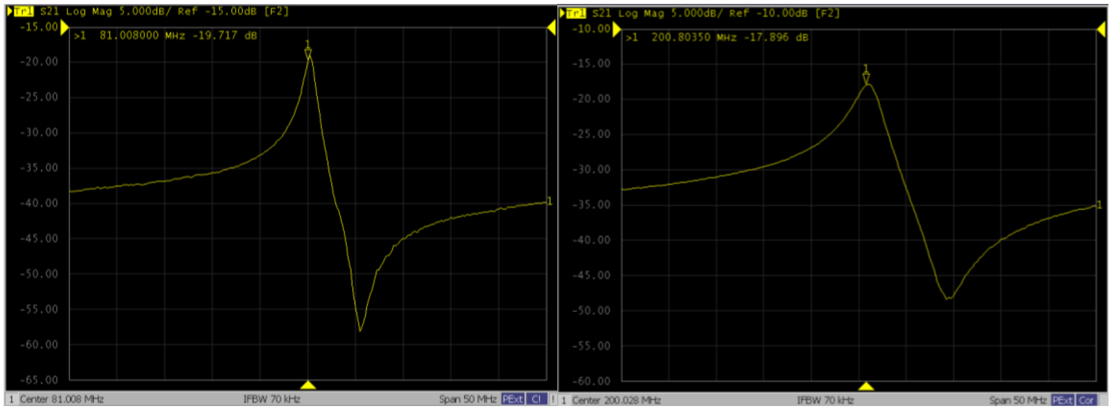

Figure 3.9 S_{21} Measurements of 4.7T Coil. Peaks show the resonant frequency of the ^{31}P coil *(left)* at 81 MHz and the ^{1}H coil *(right)* at 200 MHz. Measurements were obtained using the double-probe instrument.

The S_{21} coefficient is also called the transmission coefficient because it measures the signal response at port 2 due to a signal generated at port 1, in other words the transmission response from port 1 to port 2. To acquire the S_{21} measurements, a double-probe instrument was used, where the two probes are geometrically decoupled from each other and are plugged into ports 1 and 2. When the double-probe instrument is held near another resonant structure, the signal response sent from port 1 into probe 1 induces a current in the resonant structure. Since a current is now flowing in a resonant structure, a magnetic field is created and induces current into probe 2. The probe sends this response into port 2 creating the S_{21} measurement. In the network analyzer, this appeared as a resonant peak at a specific frequency, indicating that the energy from the incident signal leaving port 1 is deposited into the coil at that frequency. Therefore, wherever the peak is located represents the resonant frequency of the structure. This procedure was used on both the butterfly and circular loops.

Since the double-probe instrument consists of two loops that receive flux signal to obtain S_{21} measurements, it is important to consider the field patterns produced by the coils presented here. The circular loop produces field patterns as shown in Fig. 2.5. Thus, the double-probe instrument should be held perpendicular to the field pattern such that the flux direction is through the loop, as opposed to parallel with the loop. In other words it can be held directly above the loop in the same orientation.

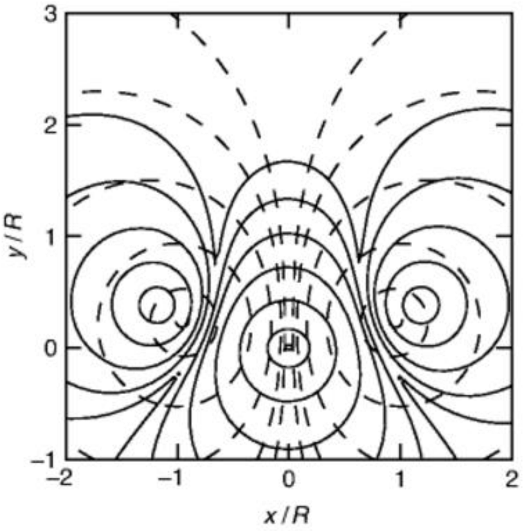

Figure 3.10 Field Patterns of Butterfly/Loop Pair. Butterfly *(solid)* and circular loop *(dashed)* field patterns are shown to be mostly orthogonal [16].

The butterfly coil produces a field pattern that is illustrated as the solid line in Fig 3.10. This image shows the field pattern of both coils as mostly orthogonal, presenting the inherent decoupling between the two structures. The field pattern directly above the center of the butterfly is in the x-direction using the coordinate axis in the figure. Thus, in order to perform S_{21} measurements on this coil, the double-probe instrument should be oriented perpendicular, such that the flux through the two probes is also in the x-direction.

Once the resonant frequencies of both loops were found, equation (3.8) was used to determine the inductances of the coils. After determining these values, the same equation is used solving instead for capacitance, and using the desired frequencies at which the coils should resonate at. Table 3.1 shows the results of this procedure. The equivalent capacitance is distributed across the coil gaps by multiplying the equivalent capacitance by the number of gaps.

It is important to note that the tuning method described above was completed before adding the tuning & matching network enclosures, baluns, and cables. This tuning step only requires the coil itself and the double-probe instrument because the coil itself does not need to be plugged into the network analyzer to obtain S_{21} measurements. Once the equivalent capacitance was found, work on building the enclosures began to allow the tuning and matching procedure to continue.

Whereas initial tuning of the coils is accomplished through S_{21} measurements, the matching process was accomplished using S_{11} measurements. These are similarly acquired through the network analyzer but require direct connections of the coil to the system. The S_{11} coefficient is also called the reflection coefficient. This is because the signal response port and signal source port are one and the same. In other words, the signal is both generated and measured at the same port (in this case, port 1). This is used to ensure that the resonant structure connected to the network analyzer is at 0 Ω reactance. Since the constructed coil has 2-channels, acquiring these measurements could be accomplished in one of two ways. First, each channel of the coil could be connected to two separate ports of the network analyzer. In this case, one signal trace on the network analyzer would represent S_{11} measurements, while the second signal trace would represent S_{22} measurements (assuming the 2nd channel was connected to port 2). The second method involves simply checking one channel at a time, in which case it is important to note that the other channel should be terminated with a 50 Ω load to simulate that channel being connected to a 50 Ω system.

Once the channel is connected to the network analyzer, Smith chart mode was used to correctly tune and match the coils. Although the coils were already tuned at this point, adjusting the variable matching capacitor changes the tuning network, modifying the resonant frequency slightly. Thus, tuning and matching at this point becomes an iterative process. To optimize the process, it is beneficial to use a Smith chart to ensure the best tuning and matching values are used. The network analyzer contains a Smith chart mode that was used during S_{11} measurements to match and tune both coils presented in this thesis. Fig. 3.11 shows the Smith chart obtained after tuning and matching the ^{31}P coil.

This tool acts as a visual representation of the coil impedance, where each loop represents a different resistance value (R, the real part of the impedance) while the marker location along the loop represents varying reactance values (X, the imaginary part of the impedance). The horizontal line along the middle of the Smith chart represents 0 Ω reactance, while the loop that intersects with the very center of the chart represents 50 Ω resistance. Thus, using the marker feature to place an indicator at the desired frequency, one can see the current impedance at that frequency, and adjust the tuning and matching capacitors as necessary until the resonant frequency is at the center of the Smith chart representing 50 Ω resistance and 0 Ω reactance. An additional benefit offered by this network analyzer is that by using a marker, the exact resistance and reactance values are shown for the frequency in question.

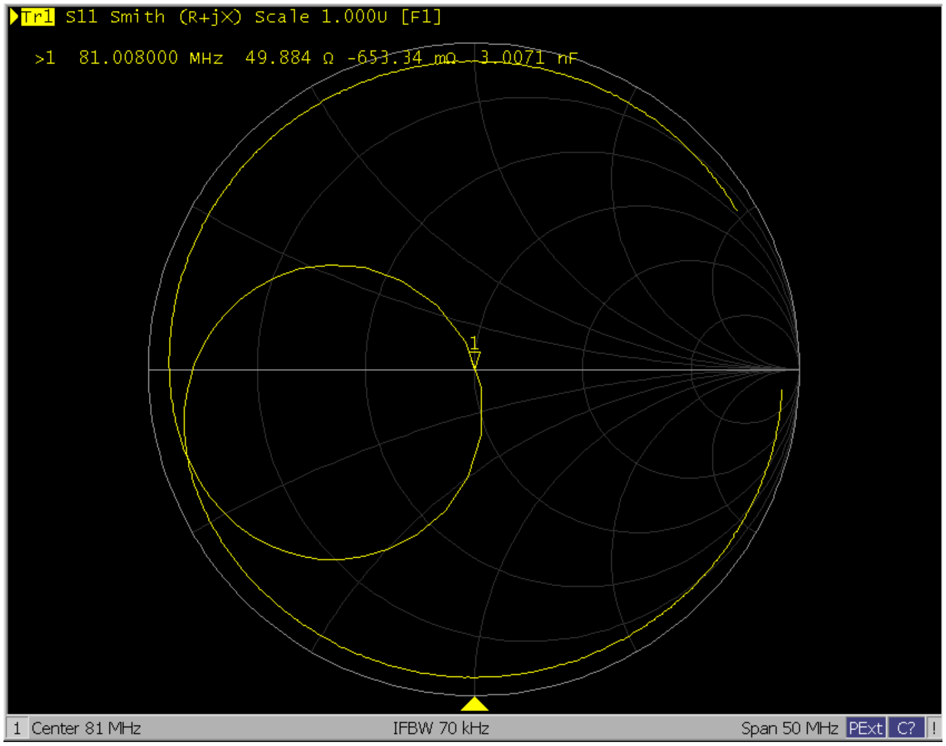

Figure 3.11 Smith Chart for ^{31}P. Smith chart showing the ^{31}P coil tuned and matched. The Smith chart shows the marker at the center, representing an impedance with 50 Ω resistance and 0 Ω reactance.

Once the coils have been tuned and matched, the network analyzer was switched back to “Log Mag” mode. This stands for the logarithm of the magnitude. This shows the amplitude of the S_{11} reflection coefficient. Since S_{11} measurements show the reflected power, the response should show a dip at the resonant frequency, signifying that maximum energy is deposited into the coil at this frequency. Fig. 3.12 shows the S_{11} curves obtained from tuning and matching the two coils. To obtain a reasonable signal, S_{11} values should be at least -20 dB at the desired frequencies.

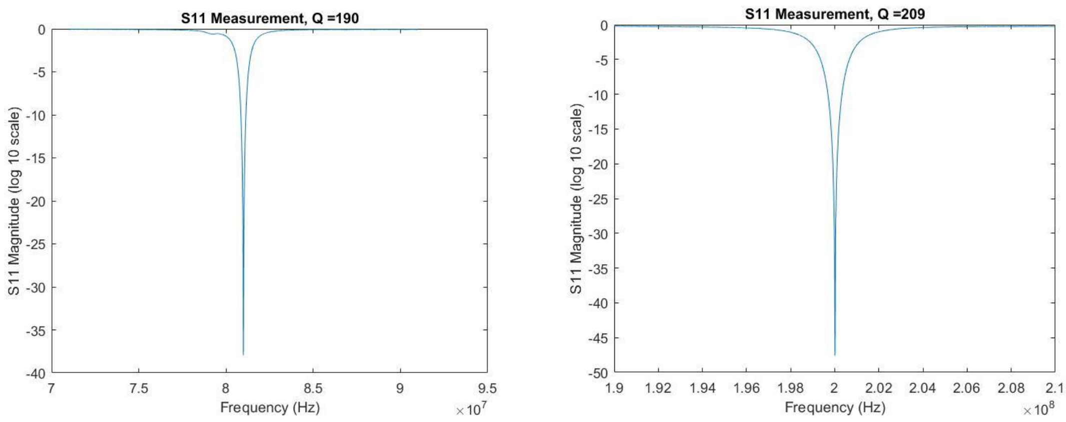

Figure 3.12 S_{11} Curves of ^{1}H and ^{31}P Channels of 4.7T Coil. The S_{11} curves are presented here for both the ^{1}H *(right)* and ^{31}P *(left)* channels. The reflection coefficients are well below the -20 dB coil standard.

III.2.2 Decoupling and Quality Factor

Once the coil has been tuned and matched, additional parameters must be measured to ensure the coil is working optimally. As described in Chapter 2, section 3.2 of this thesis, one of two priorities in creating a double-tuned coil is isolating the signal between the two channels. Without this isolation, the two coils are considered “coupled.” This undesired effect leads to interactions between the two coils where the magnetic field in one coil can induce a current in the other, leading to decreased signal amplitude or inaccurate response signals. Removing this effect is called “decoupling” and can be accomplished in many ways.

Because of the perpendicular nature of the field patterns produced by both the butterfly and circular loops in this implementation, theoretically, the coils are intrinsically decoupled. Ideally, the magnetic fields produced by one coil are not expected to induce inaccurate signals in the other. However, in practice the two coils do not produce perfectly orthogonal field patterns and still experience some coupling. Therefore, it is prudent to quantify this phenomenon and determine if the decoupling is sufficient enough to perform accurate MR experiments.

The coupling between the two coils can be quantified using S_{21} measurements, where each channel is connected to a separate port. The energy is deposited into one coil and any interaction between the two coils will cause a response at the other channel. Similar to other reflection coefficient measurements, the response is given in decibels (dB). Table 3.3 shows the results of quantifying the coupling between the two coils.

Table 3.3. Coil Coupling Between the Two Channels for the 4.7T Coil

	^{1}H coil Butterfly Loop	^{31}P coil Circular Loop
^{1}H coil	-	-36 dB
^{31}P coil	-44 dB	-

The values presented here show a very low coupling value for both coils at the other frequency. This quantification ensures that each coil can perform optimally without causing or receiving a substantial amount of signal interference from the other coil.

An additional parameter that can be quantified is the quality factor (Q). This describes the “spread” of the S_{11} curve, with larger Q values signifying a higher quality in the coil. The higher the Q value, the more energy-efficient the coil is. This means that a coil with a high Q value will dissipate energy at a lower rate than a coil with a lower Q value. An additional characteristic of a coil with high Q is that they possess a smaller range of frequencies around the resonant frequency that will also cause resonance. This is known as the bandwidth. Higher Q coils will have a smaller bandwidth and better frequency selectivity.

Obtaining Q is relatively simple once the S_{11} curves have been acquired. These values were calculated while matched and tuned to the appropriate frequencies with the -7dB S_{11} bandwidth method (24). These values were calculated for both coils. For the ^{1}H butterfly coil, Q = 209, and for the ^{31}P circular loop coil, Q = 190. When looking at these values and the S_{11} curves from Fig 3.12, it is obvious to see why the ^{31}P coil yields a larger Q as the spread of the frequencies around the resonant frequency is much smaller than that of the ^{1}H curve.

III.3 Interfacing with the Varian Inova 4.7T System

Interfacing with the Varian Inova system involved the components often referred to as the RF “front end” as these components are encountered before the receiver. Because each channel of the coil is capable of both transmit and receive modes, a transmit/receive (TR) switch was required to perform MR experiments. This component allows the system to control which mode the coil is in through trigger lines built into the component. During the MR experiment, the TR switch allow the transmit signal through to the coil during the transmit stage of the experiment, while preventing any signal response from entering into the receiver. The opposite occurs during the acquisition stage of the experiment, allowing the signal response from the coil to be acquired into the receiver while preventing any current from travelling into the coil. An existing TR switch was used and thus did not need to be created for this project.

An additional component of the RF front end is the low-noise amplifier (LNA). This is the first component encountered after the TR switch along the receive line and is used to decrease the noise and amplify the signal. Because it is the first component encountered, this is a crucial step as the receive line is considered a cascaded system where the overall noise figure is dominated by the noise figure of the first component. The placement of this component ensures an optimal signal gain and low noise figure, increasing SNR of the received signal (Miteq; 30 dB nominal gain LNA).

In performing the MR experiments, both the TR switch and the LNA need to be connected to the channel of interest. While performing experiments at this channel, it was imperative to terminate the other channel with a 50 Ω load. This maintains proper tuning and matching for the channel of interest to optimize SNR. A final step that was taken was to use a portable non-magnetic network analyzer to check the matching and tuning at the correct channel in the bore environment, ensuring once again the separate channel is terminated and ready for MRI/MRS to be performed on the 4.7T Varian Inova system.

CHAPTER IV

CONSTRUCTION OF A $^{1}H/^{31}P$ COIL AT 3T

IV.1 Design and Construction of the Multinuclear Transmit/Receive Surface Coil at 3T

This chapter describes the construction of the double-tuned coil at 3T, Stage 3 of the entire project. This coil was very similar in design to the 4.7T coil with changes in the passive components used to achieve resonance at 3T, and use of a single enclosure box to house the tuning and matching capacitor networks and the baluns for each channel. Using the same double-sided board shown in Fig. 3.2, the butterfly/loop coil was once again etched in-house using the LPKF S63 prototyping machine. The resonant frequencies along with the passive components calculated to achieve these frequencies are shown in Table 4.1. It is worth noting that the frequencies shown in the first row do not exactly equal γB_0 (where γ is the Larmor frequency and B_0 is the external magnetic field) because the Siemens manual for the 3T Verio system provides the numbers shown in Table 4.1 as the center frequencies to use for ^{1}H and ^{31}P coil calibrations to adjust for the exact B_0 value of the installed system.

Table 4.1. Resonance Requirements for $^{1}H/^{31}P$ Coil at 3T

	^{1}H Butterfly Loop	^{31}P Circular Loop
f_{res} (at 3T)	123.238 MHz	49.998 MHz
L_{coil}	61.77 nH	37.53 nH
$C_{equivalent}$	27 pF	270 pF

Once again, the equivalent capacitances were multiplied by the number of gaps in their respective coils (six for the butterfly loop and three for the circular loop) to create an even current distribution and magnetic field pattern. Variable capacitors for each channel replaced one gap (Johanson Manufacturing PN: 55H01) and allowed flexibility in tuning the coil to compensate for loading. The final values used for the passive components to achieve resonance were 27 pF capacitors at each gap for the butterfly loop (^{1}H) and 270 pF capacitors at each gap for the circular loop (^{31}P) (PassivePlus, Inc. PN: #2225C Series).

Whereas the 4.7T coil used two separate boxes for the tuning and matching networks of each channel, a more robust design using a single enclosure box for both tuning and matching networks and both baluns was used for the 3T design. As the 3T coil was intended to be used for a commercial scanner with the end-goal of independent use, this coil was designed with the end-user in mind. Therefore, design requirements such as mechanical stability, ease-of-use, and longevity played an important role in the design of the 3T coil.

The single enclosure box is the first display of these design requirements. Figure 4.1 shows a side-by-side comparison of the enclosures used in the 4.7T coil and the single enclosure of the 3T coil. The enclosure used is a non-magnetic aluminum casing with a base and a lid. A custom etched PCB board designed in Eagle and etched in-house allows the tuning and matching networks and baluns of both channels to be soldered and contained inside. PCB supports were used to elevate the board to the desired height within the box and cable strain-relief ports were added to prevent unnecessary strain from being placed on the cables potentially damaging or fraying them over time.

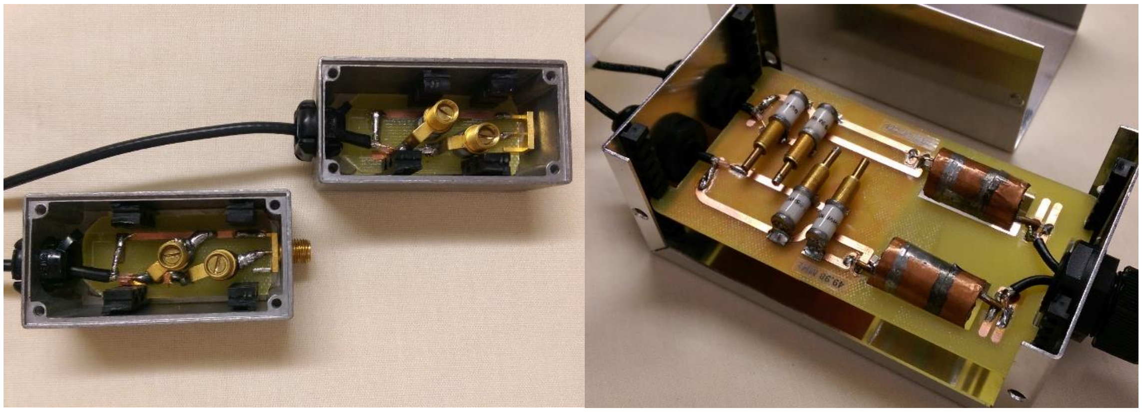

Figure 4.1 Comparison of 4.7T and 3T Enclosures. The tuning and matching networks are shown for both the 4.7T coil *(left)* and the 3T coil *(right)*. The 3T coil was designed for mechanical stability and longevity in a user-only use.

Several advantages can be observed from Fig. 4.1 such as the aesthetic appearance for the more clinical environment. The baluns are contained within the enclosed structure and cannot be seen by the user without removing the enclosure lid. Additionally, the baluns are soldered down onto the circuit within the box and do not experience strain from moving the cables they are attached to, as was the case in the 4.7T coil. Last, a lid was used to hide the electrical components and provide electromagnetic shielding.

The baluns were created using similar construction methods outlined in the 4.7T coil section on baluns but with the use of a 16.5 mm diameter PVC cylinder instead. This allowed the baluns to fit within the enclosure shown in Fig. 4.1. Another difference is seen in the terminals of the semi-rigid coax. In the 4.7T coil, SMA connectors were added to each end of the balun connecting it its adjacent components. In the 3T coil, the baluns are directly soldered onto the board within the single box enclosure, preventing any strain that may occur from removing and adding the baluns every time the coil needs to be used. To tune the baluns to the appropriate 3T frequencies, the values shown in Table 4.2 were used.

Table 4.2. Component Values of 3T Coil Baluns

	^{1}H Butterfly Loop	^{31}P Circular Loop
f_{res} (at 4.7T)	123.238 MHz	49.998 MHz
L_{balun}	308.86 nH	187.65 nH
C	5.4 pF	54 pF

The RG-174 cables that connect the baluns to the system receiver were directly soldered onto the circuit as well, instead of using SMA connectors like in the 4.7T coil. The other ends of these cables still used BNC connectors, to allow S_{11} measurements to be taken during the tuning and matching process. A sleeve was added around these two cables for ease-of-use, and to prevent entanglement during use and transportation. The sleeve was placed around the cables before they were soldered onto the board and was slipped through a strain-relief port at one end of the enclosure box. This sleeve can be seen in the final 3T coil implementation in Fig. 4.2.

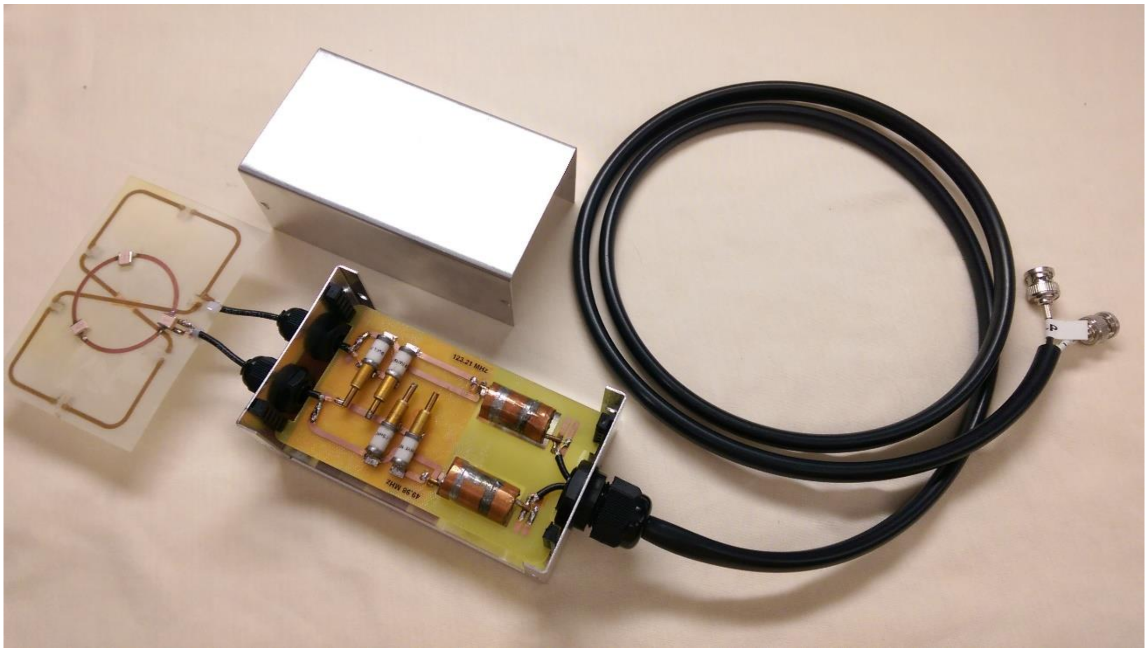

Figure 4.2 Final Implementation of 3T Coil. The double-tuned $^{1}H/^{31}P$ coil is shown at the left end along with the rest of the components for 3T imaging and spectroscopy including the tuning & matching networks, baluns, and cables. Compare with Figure 3.8, the final implementation of the 4.7T coil.

IV.2 Bench Measurements

IV.2.1 Tuning and Matching

Tuning and matching procedures follow those used on the 4.7T coil, with the main difference being the desired resonant frequencies at 3T shown in Table 4.1. Tuning was first accomplished using S_{21} measurements and a double-probe instrument. The results of these procedures are shown in Fig. 4.3.

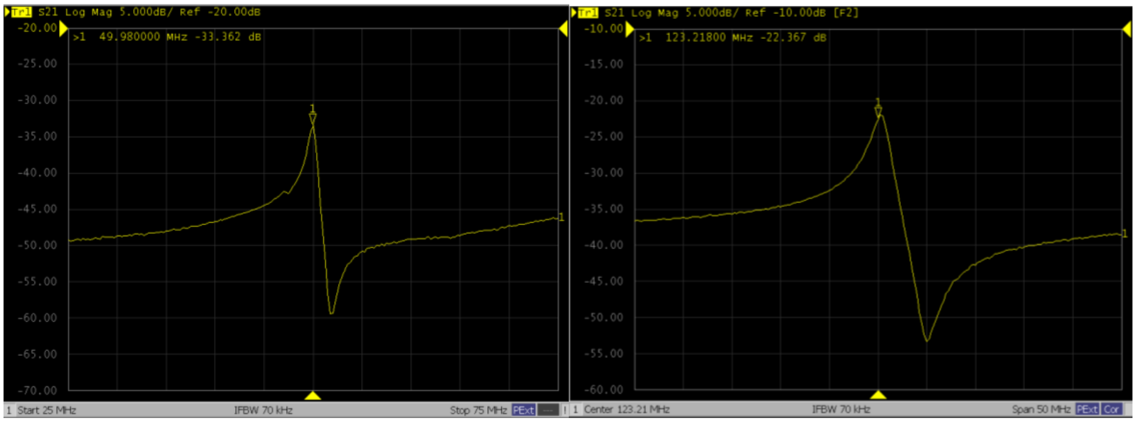

Figure 4.3 S_{21} Measurements of 3T Coil. Peaks show the resonant frequency of the ^{31}P coil *(left)* at 49.98 MHz and the ^{1}H coil *(right)* at 123.238 MHz. Measurements were obtained using the double-probe instrument.

S_{11} peaks of the two coils at the desired frequencies are shown in Fig. 4.4. Reflection coefficients for the phosphorus and hydrogen coils are -22 and -44 dB, respectively, once again meeting the -20 dB coil standard.

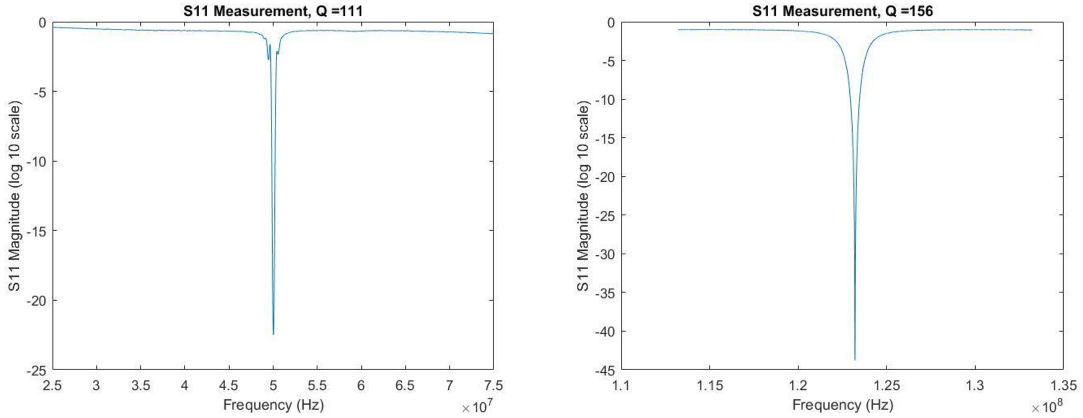

Figure 4.4 S_{11} Curves of ^{1}H and ^{31}P Channels of 3T Coil. The S_{11} curves are presented here for both the ^{1}H *(right)* and ^{31}P *(left)* channels.

IV.2.2 Decoupling and Quality Factor

Coupling measurements for the 3T coil were acquired using S_{21} measurements between each channel to ensure that the coils were decoupled enough to proceed with MR experiments. S_{21} measurements obtained between the butterfly and loop were -36 dB at ^{31}P and -40 dB at ^{1}H ensuring adequate decoupling between channels.

Table 4.3. Coil Coupling Between the Two Channels for the 3T coil

	^{1}H coil Butterfly Loop	^{31}P coil Circular Loop
^{1}H coil	-	-36 dB
^{31}P coil	-40 dB	-

Finally, Q values were also measured from the peaks in Fig. 4.4. The Q values were calculated using equation (3.10) and the S_{11} peaks in Fig. 4.4. For the butterfly coil (^{1}H) Q = 156 and for the circular loop (^{31}P), Q = 111. As with the 4.7T coil, the ^{31}P channel for the 3T coil also has a better Q-factor than the ^{1}H channel. From Fig. 4.4., these values are expected as the ^{31}P channel possesses a much more frequency selective S_{11} peak due to its narrow bandwidth.

IV.3 Interfacing with Siemens Verio 3T System

This section introduces the procedure required to interface with the Siemens Verio 3T system at the TIPS facility. The coil presented in this chapter was ultimately constructed for this scanner. Siemens commercial systems use a system of coil codes to “recognize” which coil is currently plugged into the scanner. This system is in place to ensure that each pulse sequence within the computer will only run for coils they are designed for. Each coil has a corresponding 2-digit hexadecimal code, with commercial coils possessing their own fixed coil codes. The coil codes are embedded into each coil as a set of resistors, with various resistance ranges corresponding to different hexadecimal digits. The resistance ranges and their corresponding hexadecimal codes are shown in Table 4.4.

Table 4.4. Resistor Ranges and Nominal Resistor Values for Siemens 3T Coil Codes

Code variable (hex)	Resistor, nominal values (Ω)	Resistor Ranges (Ω)
0	n.a.	n.a.
1	147	132-162
2	273	256-291
3	422	402-444
4	601	577-627
5	820	790-853
6	1090	1056-1135
7	1450	1397-1500
8	1920	1849-1989
9	2570	2478-2680
A	3560	3412-3729
B	5200	4946-5511
C	8480	7930-9207
D	18300	16259-21493
E	n.a.	n.a.
F	n.a.	n.a.

Since each coil code is 2 digits, each coil requires 2 resistors. The 2 resistors are set across a signal and ground line. Both resistors share the same ground line, leading to a total of 3 wires that connect the resistor network to the pins found in the coil connector. Once the coil connector is plugged into the scanner, the resistance values across the pin are recognized, allowing the system to read in the coil code and determine which coil is currently being used.

For the 3T coil constructed in this chapter, an existing interface box at the TIPS facility will be utilized to connect the coil to the scanner. The interface box contains several receive-line components that are shown in Fig. 4.5 along with the box itself.

Figure 4.5 Interface Box for 3T Coil. This interface box produced by RAPID MR International showing the outer casing *(left)* and the inner components *(right)*. The box contains several built-in receive-line components including TR switches for each channel, pre-amplifiers for each channel, and a frequency splitter.

In addition to these receive-line components, a set of resistors are also present within the box. Once a coil is plugged into the interface box, the resistors on the coil are placed in parallel with the resistors found within the box. Therefore, to achieve the desired coil codes, these resistor values must be taken into account when calculating which resistors to build into the coil design. The measured values of the resistors present in the box are 18.3 kΩ and 17.7 kΩ. The coil code representative of the coil that originally was designed for the RAPID MR interface box is "16." Therefore resistance ranges of 132-162 Ω and 1056-1135 Ω should be achieved at the final stage (i.e., after the coil is plugged into the interface box). Since the values of the resistors in the interface box are known, the values of the resistors that should be added to the coil's resistor network can be calculated. The values required to replicate the same coil code as the commercial coil are 148 Ω and 1163 Ω.

Thus, the next step in interfacing with the Siemens 3T scanner was the development of the resistor network and coil connector that can act as an adapter between the coil itself and the interface shown in Fig. 4.5. A preliminary model was designed in SolidWorks and 3D printed. This model houses the resistor network and allows the BNC connectors at the end of the 3T coil to be connected to the interface box. Once the adapter has been finalized, the coil can interface with the Siemens scanner and MRI/MRS experiments can be performed.

CHAPTER V

MRI AND MRS EXPERIMENTS

V.1 Phantom Development

To test the 4.7T coil capabilities, a ^{31}P phantom was created. The phantom was designed to ensure both proton (^{1}H) imaging and ^{31}P spectroscopy could be performed on it. The source of phosphorus used in this case was phosphoric acid, a source of inorganic phosphate (Pi) (Sigma Aldrich PN: #345245-100ML). To imitate physiological concentrations of Pi, a 20 mM concentration phantom was created. This number was chosen as resting Pi in mammals is approximately 1-5 mM and can rise up to 30-40 mM during intense contractions [23]. Thus, the average of the minimum and maximum possible values was taken and used for the phantom Pi concentration.

The container used was a cylinder with a 6 cm diameter to span the diameter of the ^{31}P circular loop. The phantom can be seen in Fig. 5.1 over the completed 4.7T coil. As surface coils have the best sensitivity over volumes of similar geometry and size to the coil, the phantom was chosen to ensure optimal sensitivity when performing MRI and MRS experiments.

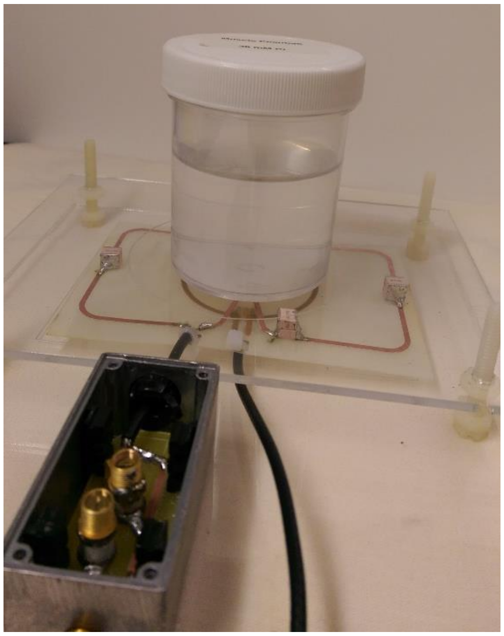

Figure 5.1 Muscle Phantom Over 4.7T Coil. The 20 mM Pi muscle phantom was created using phosphoric acid, a source of Pi.

V.2 Canine Tissue Samples

After MR experiments were performed on the muscle phantom, the next step before *in vivo* studies was testing the coil on muscle tissue samples. This would ensure that the coil could acquire signal from samples that would be of the same geometry, size, and histological composition as the *in vivo* GRMD muscle tissue.

The muscle tissue samples came from pectineus muscle groups of control and GRMD dogs of various ages. The pectineus muscle is an inner hind limb muscle found in canines. Its location in the hind limb is shown in Fig. 5.2.

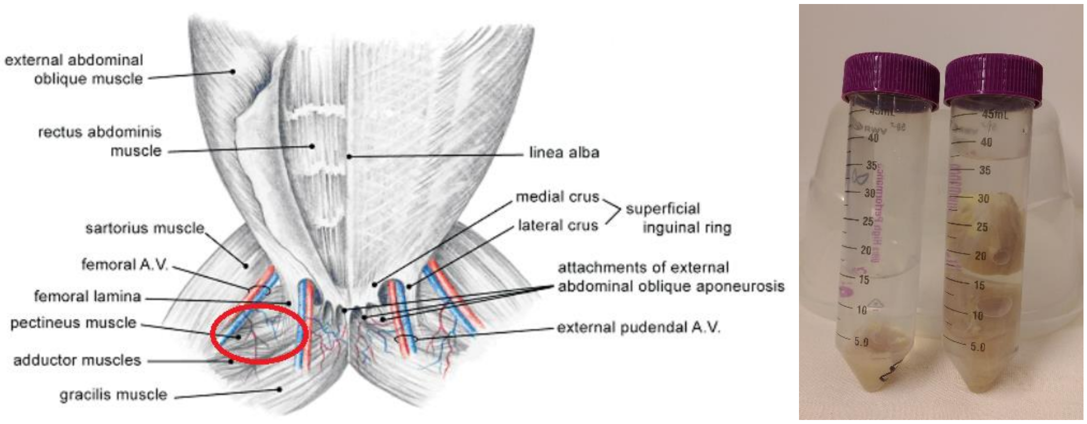

Figure 5.2 Pectineus Muscle Samples. The pectineus muscle is found in the inner hind limb of canines *(left)* [24]. Two of the eleven canine pectineus muscle tissue samples *(right)* show the diversity of the size and geometry among the samples. Tissue integrity is preserved as they are formalin-fixed after harvesting.

In total, there were 11 muscle tissue samples used in this study. They ranged in age from three months to four years old. Only two of the samples were from the control group, while the rest were from the GRMD canine population. Because of these factors, there was a large size variation among the samples, as can be seen in Fig. 5.2. In addition, four of the samples were male and the other six were female. Detailed information of each sample is shown in Table 5.1. It is important to note that the age of Sample #11 (one of the control samples) is unknown as the tissue sample was collected through a tissue share separate from the other samples.

Table 5.1. Information for Pectineus Muscle Tissue Samples

Sample #	Status	Age	Gender
1	Control	1 year	Female
2	GRMD	3 months	Male
3	GRMD	1 year	Female
4	GRMD	1 year	Female
5	GRMD	1.5 years	Female
6	GRMD	3 months	Male
7	GRMD	4 years	Male
8	GRMD	3 months	Female
9	GRMD	1.25 years	Male
10	GRMD	4 years	Female
11	Control	N/A	Female

V.3 Results

In this section, we examine the performance of the 4.7T double-tuned coil described in Chapter III. ^{31}P spectroscopy and ^{1}H imaging were both performed at 4.7T using the 40 cm Varian Inova system located in the Magnetic Resonance Lab at Texas A&M University.

V.3.1 ^{31}P Spectra

Spectroscopy of any X-nuclei requires that certain system modifications be made before MR experiments can be performed. The hardware modifications implemented include using the correct coil and also ensuring the correct quarter-wavelength transmission line is connected to the T/R switch. To ensure proper signal isolation during transmit and receive stages, a T/R switch was connected to the X-channel (in this case, the ^{31}P channel). One component of the switch is the quarter-wavelength transmission line which varies depending on the nuclei being interrogated. At 4.7T, the cable used for ^{1}H is 25 cm long while the cable used for ^{31}P is 62 cm. Once this was replaced, the hardware modifications for X-channel spectroscopy were completed. In order to hold the muscle tissue samples upright during acquisition, a small plastic container shown in Fig. 5.3 was used.

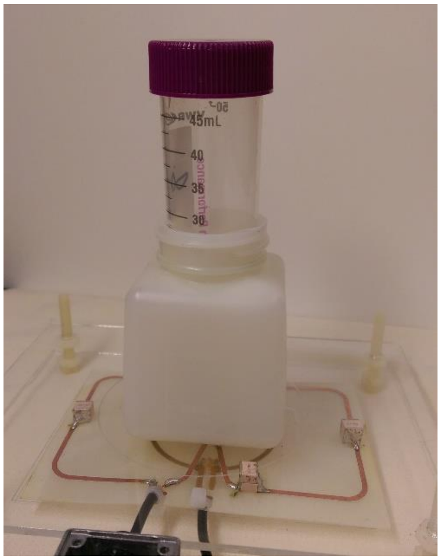

Figure 5.3 Imaging Setup for Muscle Tissue Samples at 4.7T. This small plastic container was used to hold the muscle tissue samples upright during ^{31}P spectroscopy on the Varian Inova system.

The pulse sequence used was a simple “pulse-and-acquire” sequence. This sequence is aptly named because during the sequence, the sample is excited using an RF pulse originating from the RF coil during transmit. Afterwards the RF coil enters receive mode and simply acquires the signal emitted by the sample. The same sequence was used for all ^{31}P spectral acquisitions for the phantom and samples with the following parameters: 1000 complex points over a spectral width of 10,000 Hz, TR of 2 ms. We first acquired ^{31}P spectra from the reference phantom with 20 mM Pi. As this was the first acquisition, we only used 16 transients (averages). The amplitude acquired is a relative signal, and was thus normalized to an amplitude of 1 by dividing by the maximum value of the array. Using 16 transients yielded an SNR of 21 for the reference phantom.

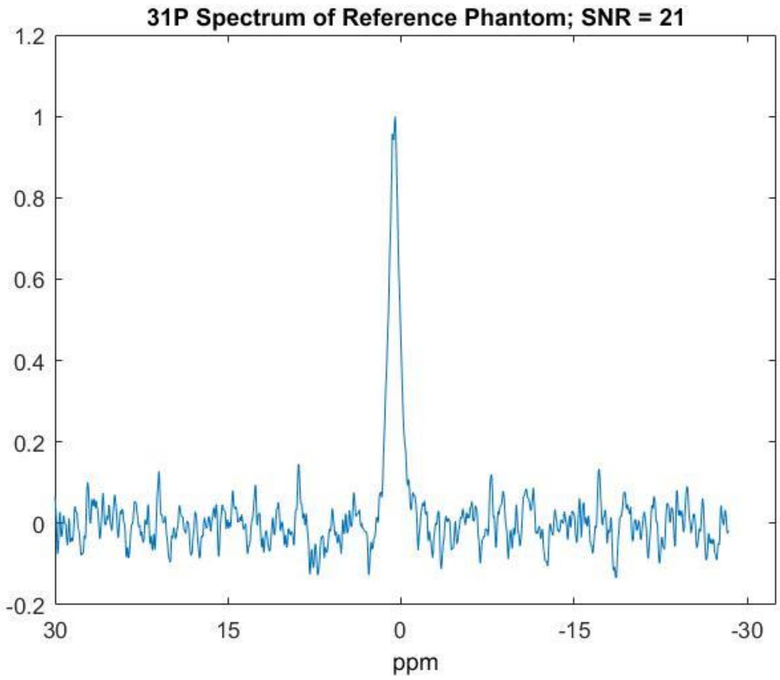

Figure 5.4 ^{31}P Spectrum of 20mM Pi Reference Phantom. The number of transients for this acquisition was 16, which yielded an SNR of 21.

After obtaining a spectrum from the reference phantom, we decided to move on to the canine muscle tissue samples. As the SNR was not optimal, we increased the number of transients first to 64 and then to 512 to observe the response, before acquiring spectra from the rest of the samples. We expected an increase in SNR, which we witnessed from the results of the spectral acquisitions of Sample #3 shown in Fig. 5.5.

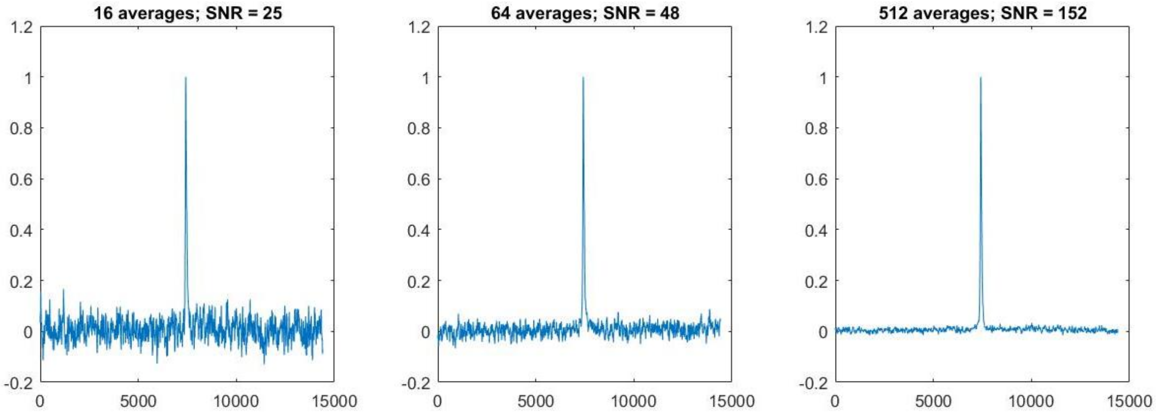

Figure 5.5 Effects of Averaging on Spectrum SNR. The SNR values for 3 different acquisitions were calculated as 25 (16 transients), 48 (64 transients), and 152 (512 averages).

Increasing the number of transients greatly increased the SNR as shown here. In fact, increasing the number of transients *n* times should theoretically increase the SNR by √*n* times. For example, in the acquisition with 16 transients, the SNR = 25. The number of transients is increased 4-fold to 64 transients, while we notice an increase in SNR that is approximately 2-fold (25 to 48). With a 4-fold increase in transients, we expected a √4-fold increase in SNR, which is observed here. The same can be shown as we increased from 64 to 512 transients to achieve an SNR of 152.

The tradeoff with increasing the number of transients lies in the total time of each acquisition. While the 3rd spectrum showed the greatest SNR, it also of course took the longest of the three acquisitions. Whereas the 1st and 2nd acquisitions took approximately one and four minutes respectively, the 512-transient acquisition took approximately 30 minutes. Thus, in the interest of time, the rest of the samples were acquired using 64 transients. In addition, spectra were acquired for samples with direct comparisons to be made (age, year, gender, or disease model). Fig. 5.5 shows the results of these spectra. Results were once again normalized based on the highest value among the spectra.

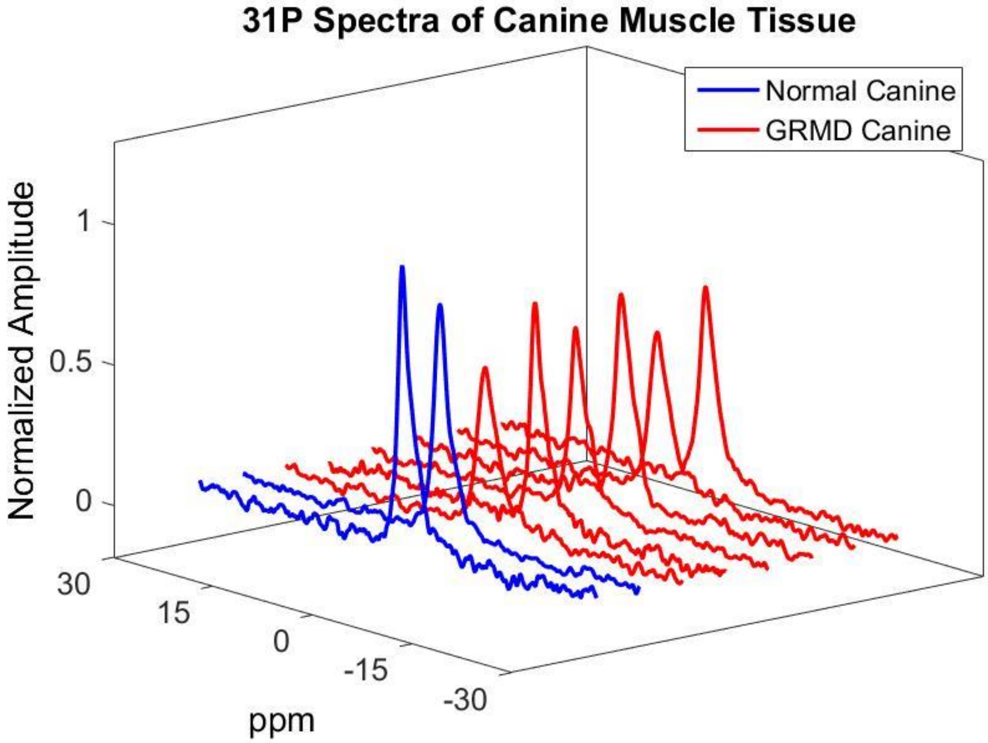

Figure 5.6. ^{31}P Spectra of Canine Muscle Tissue. This graph shows the spectra obtained from control *(Blue)* and diseased *(Red)* muscle tissue samples. The sample #'s are *(front to back)* 1, 11, 6, 2, 3, 4, 7, and 10, ordered first by disease model and then by age.

The spectra were acquired with 64 transients and show the PCr concentrations of each muscle tissue. SNR for all spectra was ~47 on average. The spectra are ordered by disease model and then by increasing age (front to back). Other compounds were not observed in the spectra, even after the 512 transients were used in Fig. 5.5. The muscle metabolites that would normally be present *in vivo* such as Pi and ATP had degraded by the point this experiment had been performed. Although ^{31}P spectra of the diseased tissue (red) present roughly the same PCr concentration, the older samples were much larger in volume. Thus, in order to obtain a fair comparison, the volumes of each sample were calculated using fluid displacement methods and are shown in Table 5.2.

Table 5.2. Volumes of Canine Muscle Tissue Samples

Sample #	**Volume (in^3)**
1	0.268
2	0.199
3	0.447
4	0.298
6	0.219
7	1.029
10	0.646
11	0.298

The spectra from Fig. 5.6 were normalized by these volumes, by dividing each data array by the corresponding volumes. This allowed us to compare PCr concentration per unit volume, as opposed to entire signal obtained. In traditional MRS experiments, a voxel is usually chosen in order to allow uniformity when acquiring data. By performing volume normalization, we accomplish a similar comparison standard. The results are shown in Fig. 5.7.

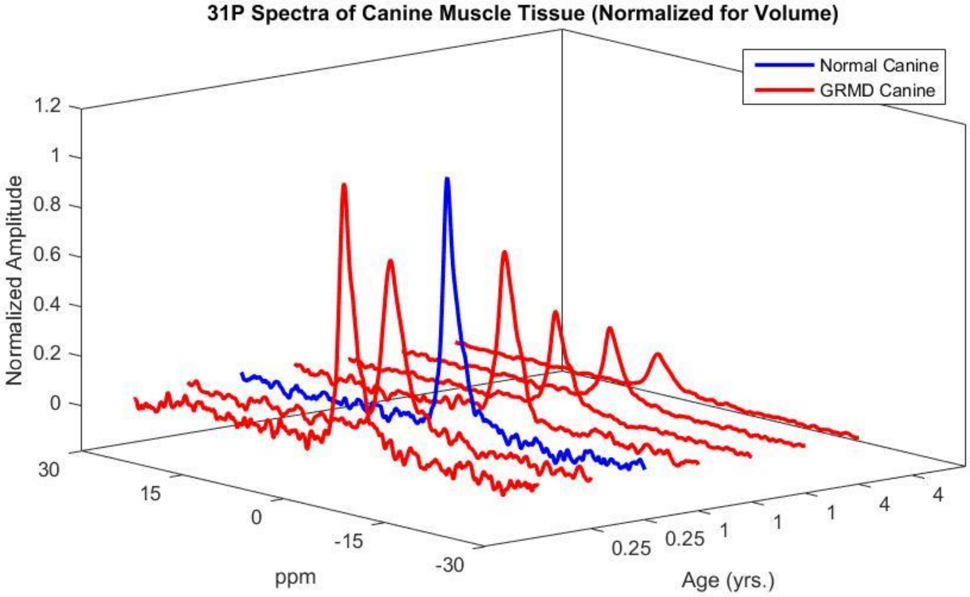

Figure 5.7. ^{31}P Spectra of Canine Muscle Tissue. These spectra are shown after normalizing for volume. They are shown in increasing age order *(front to back)* with the diseased tissue in red and the control tissue in blue.

After normalizing, two observations can be made. The diseased tissue shows a decrease in PCr concentration as the age of the canine animal model increases. Since disease progression is dependent on age, the PCr concentration decreases as the disease progresses in the GRMD animal models. In addition, the PCr concentration is shown to be higher in the normal animal model when compared to diseased tissue of the same age (1 year).

Since both the phantom and muscle tissue samples only yielded one phosphorus compound each (Pi for the phantom and PCr for the samples), an additional experiment was performed to test the coil's capabilities of obtaining spectra from multiple compounds, which would be the case *in vivo*. The 20 mM phosphoric acid phantom was placed next to sample #1 on the coil and a 16-transient acquisition was taken. Fig. 5.8 shows that the coil was able to detect signals from both PCr and Pi in a single acquisition as long as both compounds are present.

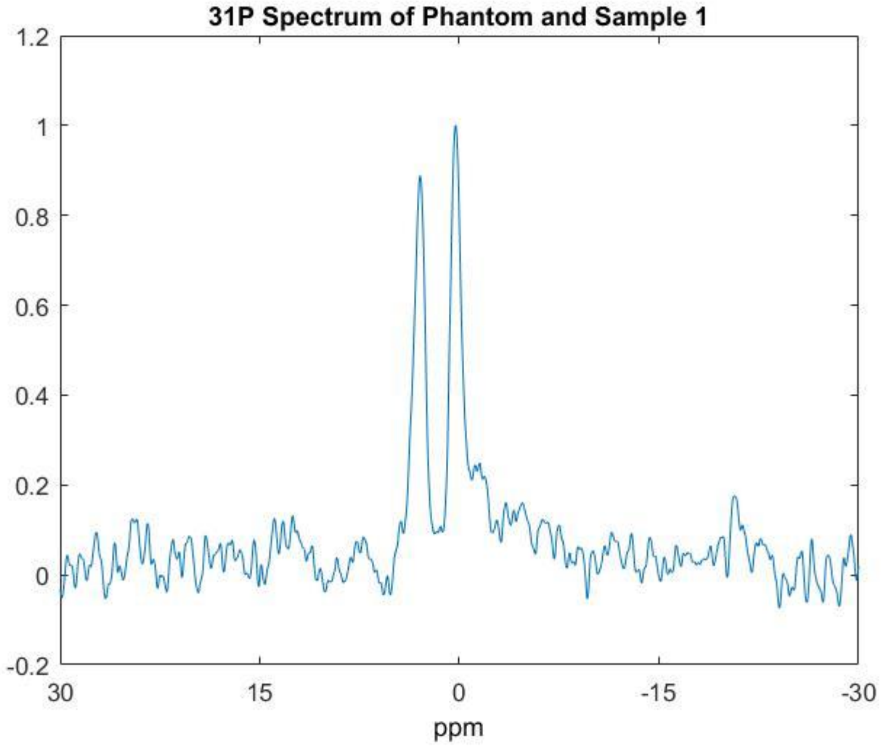

Figure 5.8 ^{31}P Spectrum of Phantom and Sample. This spectra shows the coil's capability of obtaining ^{31}P spectroscopy of multiple compounds, in this case PCr and Pi.

V.3.2 Proton Imaging

The main functionality of proton imaging for this coil is being able to obtain a scout image to confirm where ^{31}P spectroscopy is occurring in the sample. Therefore it is important to obtain localized images near the surface coil, and in the case of the muscle tissue samples, at a depth of approximately 3.5 cm. Once again, the quarter-wavelength transmission cable was replaced on the TR switch to make proton imaging possible. After switching out this cable, the ^{1}H channel was connected to the receiver and the ^{31}P channel was terminated with a 50 Ω load. An image of the muscle phantom shown was acquired to obtain a sensitivity profile of the coil.

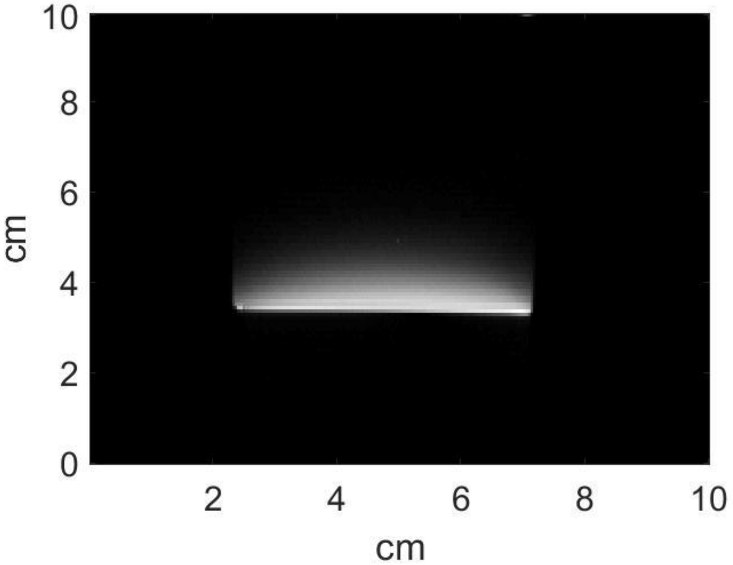

Figure 5.9 Image of Muscle Phantom. This shows the proton image of the 20 mM phosphoric acid muscle phantom. Sensitivity profile shows an imaging depth of ~3.5 cm.

The image was obtained using a spin echo sequence with the following parameters: resolution 128x128; FOV – 10x10 cm; TR = 1.5s; TE = 30ms; slice width = 2mm. The sensitivity profile shown is expected for a surface coil, with the greatest intensity closest to the coil and a signal drop off further away. An SNR map of the image was acquired by dividing each pixel of the original image by the noise, acquired by taking the standard deviation of the noise region of the image.

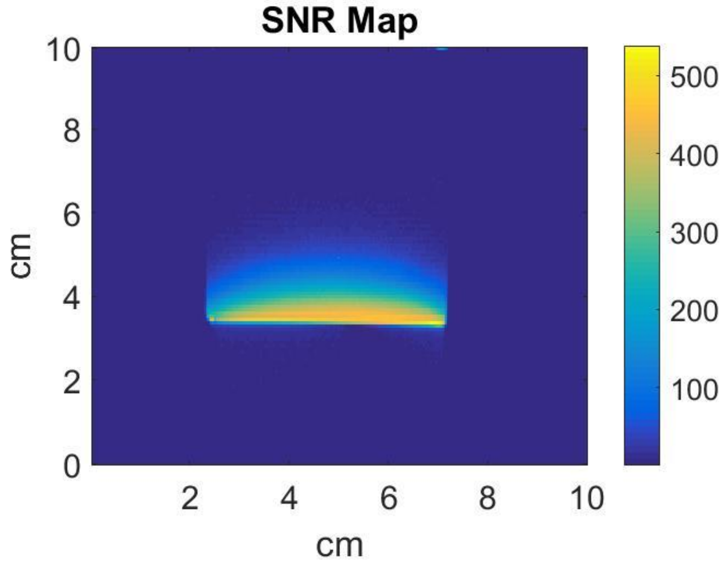

Figure 5.10. SNR Map of the ^{1}H Image. Acquired by dividing each pixel of the original image by the noise figure.

This shows values of approximately 520 nearest to the coil. Once again, a typical surface coil sensitivity pattern can be seen, with the signal closest to the coil and a signal drop off further away from the coil. As the coil is approximately 1 cm away from the coil, the SNR is expected to be adequate at the targeted imaging depth, but additional tests must be performed on canine tissue samples to validate this claim.

CHAPTER VI

CONCLUSION AND FUTURE WORK

MR spectroscopy provides a noninvasive means of characterizing the metabolites present within a sample. By quantifying key muscle metabolites such as PCr, Pi, or ATP in GRMD canine animal models through ^{31}P MRS, response to treatment can be more effectively monitored. This method is not only noninvasive, but can provide localized, accurate data relevant to characterizing the disease model without employing ionizing radiation. Without the necessary tools to perform ^{31}P MRS, data collection methods are limited to commercially available coils that have not been built to optimize SNR in smaller targeted muscle groups.

The 4.7T coil presented in this thesis was customized for this animal model to obtain ^{31}P spectroscopy and proton images with high sensitivity in a localized region. Through MRS experiments on muscle tissue samples harvested from control and GRMD populations, the 4.7T coil has been shown to be capable of obtaining localized and sensitive ^{31}P spectra using a coil size and geometry that is optimal for targeted canine muscle groups. Localized MRI was also shown to be possible up to a depth of 3.5 cm to obtain scout images prior to spectroscopy experiments. Because the coil is double-tuned, switching out different coils between experiments is not necessary, preserving the imaging setup and the ease of data acquisition.

The 3T coil presented in Chapter 4 show the next iteration of the design, prepared and intended for commercial use. Bench measurements demonstrate similar performance outcomes to that of the 4.7T coil. The variations from the 4.7T coil (aside from the frequency changes) show a more robust and structurally sound design with similar MR capabilities.

The results presented in this thesis do not attempt to draw physiological conclusions, but instead show the capabilities of the coil design presented. We have shown that the double-tuned $^{1}H/^{31}P$ butterfly/loop coil is capable of obtaining localized and sensitive hydrogen images and phosphorus spectra using a size and geometry that is optimal for targeted GRMD muscle groups. By doing so, we have opened the path for the rest of the project's stages to be completed, including interfacing the 3T coil with the Siemens system and ultimately using the coil *in vivo* on the canine animal model.

REFERENCES

[1] T. Schub, and D. Pravikoff, Muscular dystrophy, duchenne. CINAHL Nursing Guide (2015).

[2] J. Thibaud, A. Monnet, D. Bertoldi, I. Barthelemy, S. Blot, et al., Characterization of dystrophic muscle in golden retriever muscular dystrophy dogs by nuclear magnetic resonance imaging. Neuromuscular Disorders 17 (2007) 575-584.

[3] E.P. Hoffman, R.H. Brown, and L.M. Kunkel, Dystrophin: the protein product of the duchenne muscular dystrophy locus. Cell 51 (1987) 919-928.

[4] Z. Fan, J. Wang, M. Ahn, Y. Shiloh-Malawsky, N. Chahin, et al., Characteristics of magnetic resonance imaging biomarkers in a natural history study of golden retriever muscular dystrophy. Neuromuscular Disorders 24 (2014) 178-191.

[5] M.A. Cole, J.A. Rafael, D.J. Taylor, R. Lodi, K.E. Davies, et al., A quantitative study of bioenergetics in skeletal muscle lacking utrophin and dystrophin. Neuromuscular Disorders 12 (2002) 247-57.

[6] R. Lodi, G.J. Kemp, F. Muntoni, C.H. Thompson, C. Rae, et al., Reduced cytosolic acidification during exercise suggests defective glycolytic activity in skeletal muscle of patients with Becker muscular dystrophy: an in vivo 31P magnetic resonance spectroscopy study. Journal of Neurology 122 (1999) 121-130.

[7] J.T. Vaughan, and J.R. Griffiths, RF coils for MRI. Wiley, Chichester, 2012.

[8] M. Puddephat, Principles of magnetic resonance imaging. VoxelCube, 2002.

[9] M. Albert, Magnetization and polarization, Harvard Medical School Department of Radiology. 2006.

[10] T.B. Rodrigues, J. Valette, and A.K. Bouzier-Sore, 13C NMR spectroscopy applications to brain energy metabolism. Frontiers in Neuroenergetics 5 (2013) 9.

[11] J.C. Lindon, and I.D. Wilson, 19F NMR spectroscopy: applications in pharmaceutical studies. eMagRes 4 (2015) 189–196.

[12] B.J. Clark, M.A. Acker, K. McCully, H.V. Subramanian, and R.L. Hammond, In vivo 31P-NMR spectroscopy of chronically stimulated canine skeletal muscle. American Journal of Physiology 2 (1988) 258-266.

[13] J.F. Dunn, I. Tracey, and G.K. Radda, A 31P-NMR study of muscle exercise metabolism in mdx mice: evidence for abnormal pH regulation. Journal of the Neurological Sciences 113 (1992) 108-113.

[14] J.L. Thibaud, N. Azzabou, I. Barthelemy, S. Fleury, L. Cabrol, et al., Comprehensive longitudinal characterization of canine muscular dystrophy by serial NMR imaging of GRMD dogs. Neuromuscular Disorders 22 (2012) 85-99.

[15] K. McCully, F.G. Shellock, W.J. Bank, and J.D. Posner, The use of nuclear magnetic resonance to evaluate muscle injury. Medicine & Science in Sports & Exercise 24 (1992) 537-542.

[16] A.W. Magill, and R. Gruetter, Nested surface coils for multinuclear NMR. eMagRes (2011).

[17] W.Y. Chiang, and M.P. McDougall, Streamlined construction of a six-channel mouse array coil with 3D-printing. 24th Proc. Intl. Soc. Mag. Reson. Med., 2015.

[18] C.E. Hayes, and L. Axel, Noise performance of surface coils for magnetic resonance imaging at 1.5 T. Med. Phys. 12 (1985) 604-607.

[19] Bader, R., An introduction to the electronic structure of atoms and molecules. McMaster University Chemistry Department.

[20] B.L. Beck, Double-tuned surface coils. eMagRes (2011).

[21] A. Kumar, and P.A. Bottomley, Optimized quadrature surface coil designs. MAGMA 21 (2008) 41-52.

[22] X. Yang, T. Zheng, and H. Fujita, T/R switches, baluns, and detuning elements in MRI RF coils. 14th Proc. Intl. Soc. Mag. Reson. Med., 2006.

[23] D.G. Allen, and H. Westerblad, Role of phosphate and calcium stores in muscle fatigue. The Journal of Physiology-London 536 (2001) 657–665.

[24] M.R. Beittenmiller, F.A. Mann, G.M. Constantinescu, and J.K. Luther, Clinical anatomy and surgical repair of prepubic hernia in dogs and cats. Journal of the American Animal Hospital Association 45 (2009) 284-290.